Application of Diamond Based Beam Loss Monitors at LHC

DESY Zeuthen

and

Brandenburg University of Technology

and

CERN

Supervisor
Prof. Dr. Wolfgang Lohmann
Prof. Dr. Rüdiger Schmidt

Maria Hempel

April 4, 2013

Selbstständigkeitserklärung

Hiermit bestätige ich, Maria Hempel, dass die vorliegende Arbeit selbstständig und unter Verwendung der angegebenen Quellen und Hilfsmittel angefertigt wurde.

Genf, den 22.10.2012

Maria Hempel

Contents

1 Introduction

The Large Hadron Collider (LHC) was conceived in the 1980s and started the operation in 2008. It needed more than 20 years to plan and construct this accelerator and its experiments. Four main experiments are located around the ring, **C**ompact **M**uon **S**olenoid (CMS), **A** **T**oroidal **L**HC **A**pparatu**s**(ATLAS), **A** **L**arge **I**on **C**ollider **E**xperiment (ALICE) and **LHC** **b**eauty (LHCb). Two beams that traveling in opposite direction in the LHC tunnel, collide in each of the experiments to study the questions: "What is mass?", "What is the universe made of?" and "Why is there no antimatter?".

The four experiments take data of the collision products and try to answer the fundamental questions of physics. The two larger detectors, CMS and ATLAS, are looking for the Higgs boson to study the electroweak symmetry breaking. Both detectors were built with contrasting concepts to exclude potential error sources and to reaffirm the results. The smaller experiment LHCb studies the matter-antimatter asymmetry with a focus of the beauty quark. Another smaller experiment is ALICE that studies the conditions right after the Big Bang by colliding heavy ions.

The navigation of the beams is done by over 10000 magnets and each beam has a stored energy of 362 MJ which correspond to the kinetic energy of a train like the TGV travelling of 150 km/h [1]. Only a small percentage of that energy can damage the material in the LHC ring or the magnets. This would mean a repair time of months or years, without taking any data. To avoid such a scenario, it is important to monitor the beam condition and measure the amount of losses of the beam. Such losses can for example happen due to dust particles in the vacuum chambers or due to deviations of the beam parameters.

Several systems called beam loss monitors (BLMs) can measure beam losses. This thesis concentrates on two of them, ionization chambers and diamond detectors. Both types of beam loss monitors are explained in Sec. 3.5. Over 3600 ionization chambers are installed in the LHC, especially near each quadrupol and next to collimators. Ionization chambers have a time resolution of 40 μs that is a half LHC turn and in case of a large beam loss, they request a beam dump.

Another type of beam loss monitors are diamond sensors because of a time resolution of about one nanosecond and high radiation hardness. One diamond detector system is located in the cleaning region of the LHC and is able to detect various types of beam losses. Another diamond detector system (BCM1F) is installed inside the CMS detector to protect the CMS from adverse beam conditions. BCM1F monitors also the luminosity during collisions and delivers important beam parameters. Additional condition monitors, based on the BCM1F system, are located next to CMS, near to LHCb and ALICE to measure large beam losses in the LHC ring.

Section 6 explains the process of a beam loss due to dust particles and additional simulations were done to understand these process in more detail. The result of the simulation are also given in the same section.

Beam loss data recorded by the diamond sensors in the cleaning region and the BCM1F diamonds are presented in Section 8.

2 Kurzfassung

Der Large Hadron Collider (LHC) wurde in den 80er Jahren konzipiert und startete seinen ersten Betrieb in 2008. Es brauchte mehr als 20 Jahre um den Beschleuniger und die dazugehörigen Experimente zu planen und zu bauen. Vier Hauptexperimente befinden siche um den Beschleunigerring, **C**ompact **M**uon **S**olenoid (CMS), **A** **T**oroidal **L**HC **A**pparatus(ATLAS), **A** **L**arge **I**on **C**ollider **E**xperiment (ALICE) and **LHC** **b**eauty (LHCb). Zwei Strahlen mit geladenen Teilchen (Protonen oder schwere Ionen) bewegen sich in gegensätzlicher Richtung im LHC Tunnel, um in den Experimenten zur Kollision gebracht zu werden. Die Experimente sollen folgende Fragen beantworten:“Was ist Masse?”, “Woraus besteht das Universum?” und “Warum befindet sich im Universum keine Antimaterie mehr?”.
Die vier Experimente nehmen Daten von den Kollisionsprodukten und versuchen die fundamentalen Fragen der Physik zu beantworten. Die zwei größren Experimente, CMS und ATLAS, suchen nach dem Higgs Boson und erforschen die Elektroschwache Symmetriebrechung. Beide Detektoren wurde mit unterschiedlichen Konzepten erbaut, um potentielle Fehlerquellen auszuschließen und die Ergebnisse gegenseitig zu bestätigen. Das kleinere Experiment LHCb untersucht die Materie-Antimaterie Asymmetrie mit dem Focus auf das Beauty Quark. Ein weiteres kleineres Experiment ist ALICE, welches die Bedinungen direkt nach dem Urknall untersucht. Diese Untersuchungen erfolgen bei der Kollisonen mit schweren Ionen.
Die Navigation der Teilchenstrahlen wird durch über 10000 Magnete realisiert. Jeder einzelne Teilchenstrahl hat eine gespeicherte Energie von 362 MJ, was der kinetischen Energie von einem TGV mit 150 km/h gleicht. Allein ein kleiner Prozentsatz von dieser Energie kann Material im LHC Ring oder Magnete beschädigen. Das würde eine Reparatur zur Folge haben, die Monate oder Jahre andauern kann, sodass die Experiment keine Daten nehmen könnten. Um solch ein Szenario zu verhindern ist es wichtig die Teilchenstrahlbedingungen zu beobachten, die Verluste des Strahles zu verfolgen und deren Betrag zu messen. Solche Strahlverluste können durch Staubteilchen in den Vakuumkammern oder durch Abweichung der Strahlparameter passieren.
Verschiedene Deketorsysteme können diese Strahlverluste messen. Diese werden auch ’beam loss monitors’ (BLMs) genannt.
Diese Arbeit wird sich auf zwei von ihnen konzentrieren - Ionisationskammern und Diamantdetektoren. Beide Arten von Monitoren werden im Kapitel 3.5 erklärt. Über 3600 Ionisationskammern sind im LHC installiert, besondere Stellen sind dabei Quadrupole und Kollimatoren. Ionisationskammern haben eine Zeitauflösung von 40 μs, was einem halben LHC-Umlauf entspricht. Im Falle von großen Strahlverlusten wird der Strahl unterbrochen und abgeschaltet.
Andere Strahlverlustmonitore nutzen Diamanten als Sensoren, die aufgrund ihrer hohen Zeitauflösung von etwa einer Nanosekunde und ihrer Strahlhärte verwendet werden. Ein Diamantensystem befindet sich in der Cleaning Region des LHC und kann verschiedene Arten an Strahlverlusten sehen. Ein weiteres System aus Diamanten (BCM1F) ist im CMS installiert, um CMS vor ungünstigen Strahlbedingungen zu schützen. BCM1F beobachtet auch die Luminosität während Kollisionen aufgezeichnet werden und liefert wichtige Strahlparameter. Zusätzliche Diamantdetektoren, basierend auf dem BCM1F System, wurden noch neben CMS, LHCb und ALICE platziert um, Strahlverluste über den gesamten LHC Ring zu beobachten. Kapitel 6 erklärt den Prozess, wenn ein Staubteilchen in den Strahl fällt. Simulationen wurden gemacht um dieses Phänomen im Detail zu verstehen. Die Resultate dieser Studie werden auch in der Arbeit gezeigt.

Daten von Strahlverlusten, welche von den Diamanten in der Cleaning Region und von den BCM1F Diamanten gemessen wurden, werden im Kapitel 8 präsentiert.

3 The Large Hadron Collider

3.1 Layout of the Large Hadron Collider

The LHC at CERN is a particle accelerator and storage ring that collides two counter rotating beams (beam 1 travels anti-clockwise and beam 2 clockwise). It is located about 100 m underground at the boarder of France and Switzerland. The LHC is installed in the tunnel of the previously used Large Electron Positron accelerator (LEP). The circumference of the LHC ring is 27 km and it consists of eight octants that are also called insertion region (IR1, IR2,..., IR8). The octants are illustrated in Fig. 1(a). Each octant has a straight section. In the straight section the four experiments and the four LHC accelerator systems are installed. Two accelerator systems contain the beam collimation to absorb beam losses and the other two contain the beam dumping system and the radio-frequency (RF) accelerating system.

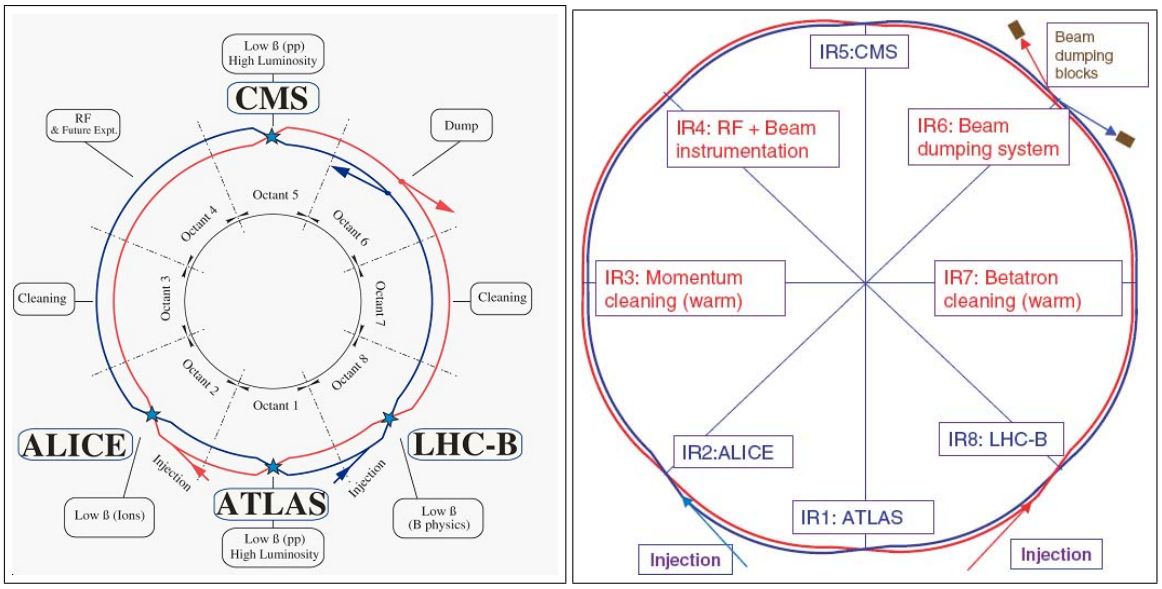

(a) Illustration of octants in LHC ring

(b) Schematic layout of the LHC ring

Figure 1: Scheme of the LHC ring. The LHC has four experiments (ATLAS, ALICE, CMS and LHCb) and four acceleration systems (momentum cleaning, RF, dumping system and betatron cleaning). The two injection points are at ALICE and LHCb.

The beams intersect at the interaction point (IP) of the four experiments (IP1 in ATLAS, IP2 in ALICE, IP5 in CMS and IP8 in LHCb) as shown in Fig. 1(a) and Fig. 1(b). The duration of a data taking period with collision is around 10 h and at the end the beams will be extracted via transfer lines from the LHC to the beam dumping system into beam absorbers. Close to the experiments ALICE and LHCb, the injection for the the beams takes place.

The straight sections are connected to an arc section that includes the dipole magnets as indicated in Fig. 1(b).

The LHC ring was built to accelerate protons and heavy ions. The proton beams can reach a

nominal momentum of 7 TeV/c with a nominal luminosity[1] of $10^{34}\,\mathrm{cm}^{-2}\mathrm{s}^{-1}$ and each beam has a stored energy of 362 MJ that correspond to 100 kg of TNT [1]. Today, the LHC operates at a momentum of 4 TeV/c with a luminosity of $7 \cdot 10^{33}\,\mathrm{cm}^{-2}\mathrm{s}^{-1}$.
Each beam has several packets of particles that are called bunches. The minimum time between two bunches is 24.95 ns for the nominal settings. Today, an operational spacing of ~ 50 ns is used. One bunch contains $1.15 \cdot 10^{11}$ protons and needs 89 μs for one LHC turn. Multiple bunches form a bunch train that lasts a few μs [2]. All in all, $3.2 \cdot 10^{14}$ protons, corresponding to 2808 bunches, can be accelerated in the LHC ring. With the bunch spacing of 50 ns it is possible to accelerate 1380 bunches. The beams have a particle free abort gap to ensure that all particles can be extracted from the LHC ring using a fast magnet without any uncontrolled particle loss. The abort gap is 3 μs long which correspond to the rise time of the dump kicker magnets used to deflect the beams in the beam dump. The scheme of the beam pattern is illustrated in Fig. 2.

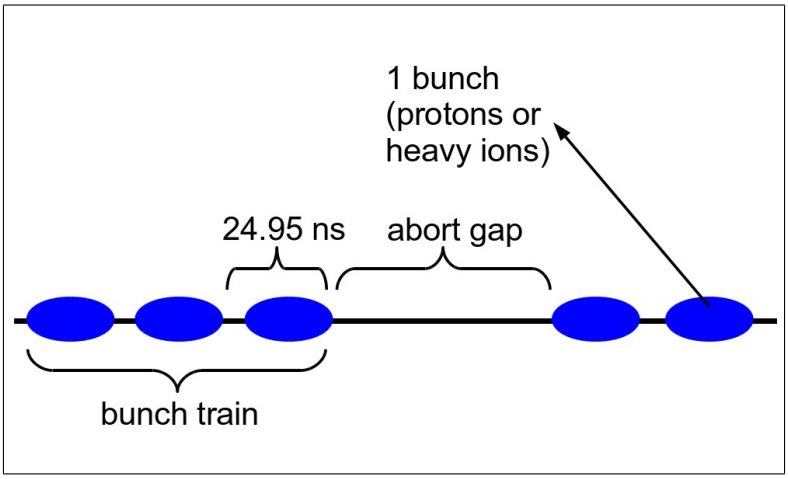

Figure 2: Scheme of the LHC bunch structure. One bunch train consists of multiple bunches and the minimum bunch spacing is 24.95 ns. The time of the particle free abort gap is 3 μs that corresponds to the rise time of the beam dump kicker magnets.

3.2 The LHC Pre-Accelerators

To accelerate the particles to the LHC injection energy of 450 GeV, several pre-accelerators are needed. The whole complex of accelerators is shown in Fig. 3. The protons, that are coming from a hydrogen source, are accelerated in the Linear Accelerator 2 (Linac 2) to 50 MeV and transferred to the Proton Synchrotron Booster (PSB) that has four rings. In the first cycle all PSB rings are filled and in a second cycle only two PSB rings. Bunches in the PSB rings are accelerated to 1.4 GeV and transferred to the Proton Synchrotron (PS). The PS is filled up first with four bunches from all PSB rings and after 1.2 s a second cycle with two bunches fills the PS [3]. At the end, 6 bunches circulate in the PS. The 6 bunches in the PS are split into 18 and accelerated to 25 GeV. After the acceleration, the bunches are split into 36 bunches and finally into 72 bunches (nominal parameters). More information about splitting and injection scheme can be found in Ref. [4]. However, one empty bunch is sent from PSB to the PS. Therefore, 12 of the final 84 bunches after the splitting are empty which correspond to an abort gap of 320 ns. That gap is

[1] Luminosity is proportional to the rate of collisions and depends on the beam size, the number of bunches and number of particles per bunch (see Sec. 7.4).

needed for the rise time of the PS ejection kicker that finally transfers all the 72 proton bunches to the Super Proton Synchrotron (SPS). Three or four cycles from the PS are required to fill up the SPS with a bunch number of 216 or 288 bunches (described in Ref. [4]). The SPS can accelerate the 216/288 bunches to 450 GeV and fills up each LHC ring with 2808 bunches within 12 cycles. Two transfer lines for the two LHC rings are needed to transfer two beams that rotate in opposite directions. At the end of the transfer lines kicker magnets are pulsed with high voltage to deflect the beams into the LHC ring. Both rings are filled up within 24 SPS cycles in total [5]. In the two LHC rings the bunches are accelerated to a nominal energy of 7 TeV.

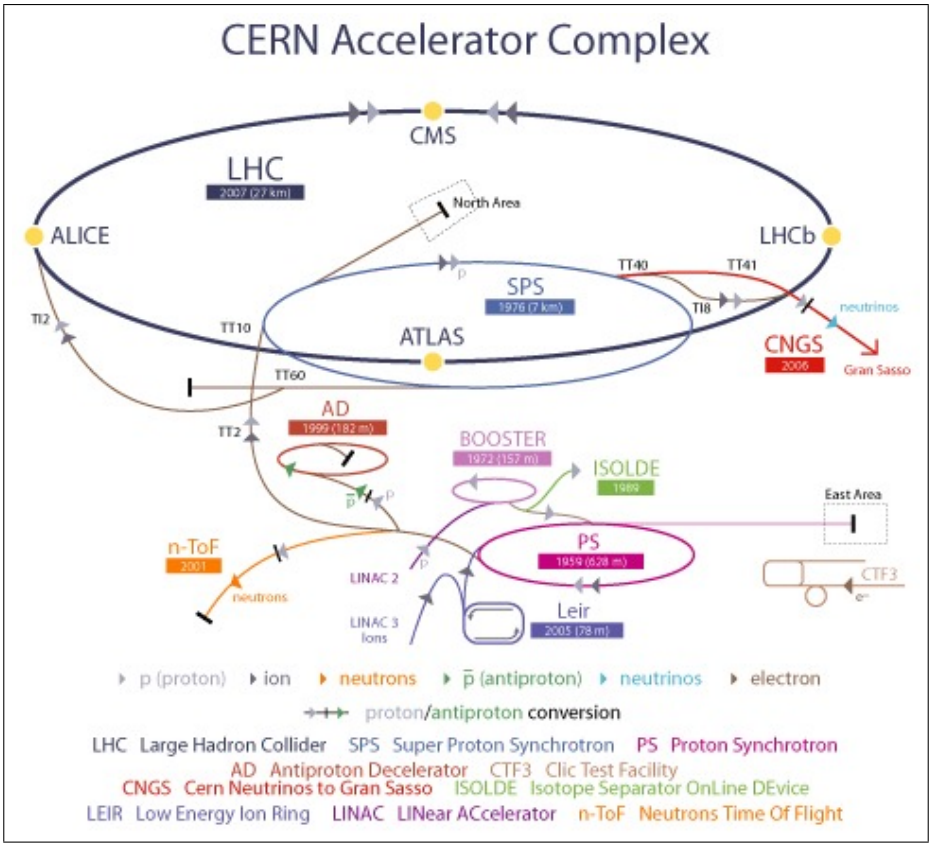

Figure 3: Accelerator complex of the LHC. Four pre-accelerators (LINAC 2, PSB, PS and SPS) are needed to inject particles in the LHC ring.

3.3 Magnets

Synchrotrons may have a complicated shape with alternately arc and straight line sections. A nominal trajectory of the particles is needed to ensure that none of the particles is crossing the vacuum chamber and is lost. The steering and focusing of the beam is done by magnets. Also an electrical field is possible because an electrical field has the same effect on the beam as a magnet field ($\overrightarrow{E} = c \cdot \overrightarrow{B}$) if we assume that $v = c$ for particles in a synchrotron. However, for a magnetic field of 1 T, that is easy to produce, a corresponding electrical field of $3 \cdot 10^8\,\mathrm{Vm}^{-1}$ is beyond the technical limits [6].

The most important magnets in a ring accelerator are dipoles. The dipoles ensure the beam steering around the ring and the bending force is adjusted to obtain a nominal bending radius R.

A sector magnet, very often used in accelerators, is a special dipole. The particle enters and leaves the dipole with 90° as illustrated in Fig. 4.

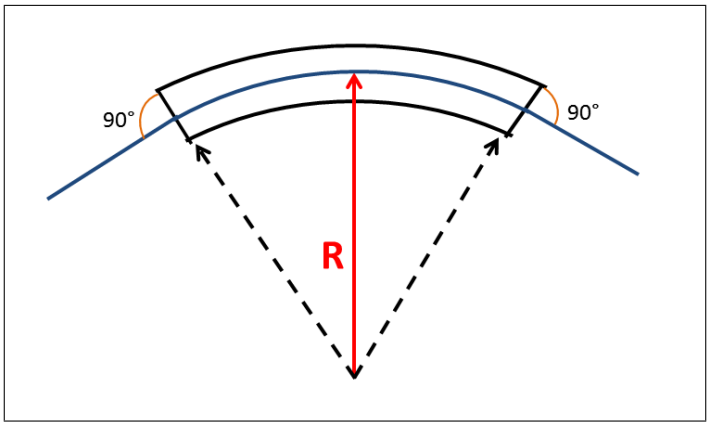

Figure 4: Effect of a sector magnet on a particle. The particle enters and leaves the magnet with 90°.

We now calculate the magnetic field of the dipole that deflects the particle with the bending radius R since we need it in Sec. 4.
We assume a Cartesian coordinate system $K = (x, z, s)$ with s as the beam direction of a ring. If a particle moves parallel to s with the velocity $v = (0, 0, v_s)$ and the magnetic field has only the components $\overrightarrow{B} = (B_x, B_z, 0)$, the Lorentz force is then

$$\overrightarrow{F} = q\left(\overrightarrow{v} \times \overrightarrow{B}\right) \tag{3.1}$$

$$F_x = -q \cdot v_s \cdot B_z \ . \tag{3.2}$$

That force has to be equivalent to the centrifugal force to keep particles on the track.

$$F_R = \frac{m \cdot v_s^2}{R} = F_x \ , \tag{3.3}$$

where m is the mass of the particle. After using $p = m \cdot v_s$, we get a relation between bending radius and magnetic field of the dipole:

$$\frac{1}{R\,(x, z, s)} = \frac{q}{p} \cdot B_z\,(x, z, s) \ .$$

If we expend the magnetic field around the nominal trajectory, multipoles become important and the magnetic field is a sum of all multipoles (Taylor series):

$$B_z = B_{z_0} + \frac{dB_z}{dx} \cdot x + \frac{1}{2!}\frac{d^2B_z}{dx^2} \cdot x^2 + \dots \ ,$$

multiplied by q/p, we get

$$\begin{aligned} \frac{q}{p}B_z\left(x\right) &= \frac{q}{p}B_{z_0} + \frac{q}{p}\frac{dB_z}{dx}x + \frac{1}{2!}\frac{q}{p}\frac{d^2B_z}{dx^2}x^2 + \dots \\ &= \underbrace{\frac{1}{R}}_{\text{dipole}} + \underbrace{kx}_{\text{quadrupole}} + \underbrace{\frac{1}{2!}lx^2}_{\text{sextupole}} + \dots \end{aligned} \tag{3.4}$$

Equation 3.4 illustrates the needed mutlipoles for particles on a trajectory displaced from the ideal one. Dipoles are needed to bend the particle around the ring, quadrupoles focus the beam and higher multipoles compensate for example the field errors and the chromaticity (an explanation of chromaticity is given in Sec. 4.2).
Quadrupoles can either focus the beam in the horizontal or in the vertical plane, therefore, two different types of quadrupoles are needed in accelerators (focusing and defocusing quadrupoles) [7]. The magnetic field of a quadrupole is illustrated in Fig. 5.

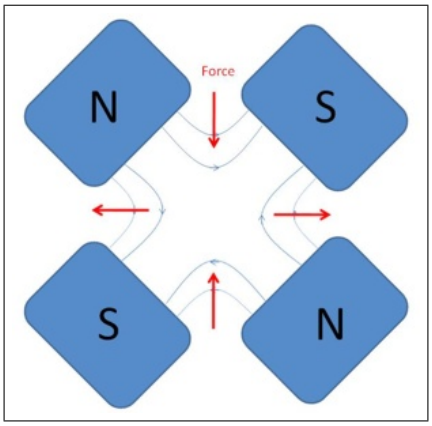

Figure 5: Magnetic field of a vertically focussing quadrupole.

If a particle deviates from the center of the beam in the vertical direction of the quadrupole axes, it is deflected back to the center of the magnet and focused, as can be seen in Fig. 5. However, the particles are defocussed in the horizontal plane. A rotation of the quadrupole by 90° causes a focusing in the horizontal plane and a defocusing in the vertical plane. Therefore, a combination of both types of quadrupoles are used to achive focusing in the horizontal and vertical plane.
Typically, magnets are made of iron. The magnetic field B, induced by a current I through the magnet coil, holds

$$B \sim I \tag{3.5}$$

for a field strength up to $\sim 1\,\mathrm{T}$. Above 1 T the dependence of the field strength on the current becomes non-linear and a saturation occurs at about 2 T. However, a magnetic field of 2 T is not sufficient for proton accelerators as the LHC. With a nominal proton energy of 7 TeV, a dipole field of 8.33 T is needed [8]. Only superconducting magnets can generate such a high magnetic field. Superconductivity is a phenomenon of several materials. The resistance becomes zero when they are cooled down below a critical temperature. Some materials with a good conductivity at room temperature, for example copper, are not superconductive even at 0 K. Usually superconductors

have to be cooled down with helium to reach a temperature close to 0 K. The magnets in the LHC are made of NbTi with a critical temperature of 9.2 K. The operation temperature of the magnets in the LHC is around 2 K that can only be reached with superfluid helium [9].
Above the critical temperature, the superconductor becomes normal conducting. The transition from the superconducting to normal conducting state is called magnet quenching. It happens when the temperature of the magnet becomes higher than the critical temperature. Such a magnet quench due to heating has several reasons, e.g. a failure in the cooling system or energy deposition in the order of mJ/cm^3 caused by beam losses. Beam losses cannot be avoided during the operation of the LHC, e.g. large beam losses during injection from the SPS to the LHC ring. Therefore, it is important to measure them and to understand the mechanisms of different types of beam losses and minimize them.

3.4 Collimators

Beam losses are unavoidable in the LHC ring and must be captured by a collimation system to prevent for example superconducting magnet quenches during operation or after beam dump. The collimators protect also the elements and material of the machine against damage due to high intensity beams that for example become unstable which leads to beam losses. Another reason for the need of collimators is to capture beam halo that are particles transported out from the core of the beam due to small energy or angular deviations. Such beam halo particles are regular beam losses and cannot be avoided. Several regular beam losses are described in more detail in ref. [10]. However, also machine failures during injection, extraction or operation can lead to large losses which has to intercept by the collimators. One failure could be the pre-firing of the injection kicker magnets which causes an accidentally deflection of the beam. In these cases, collimators and absorber can protect the LHC material from major beam losses.
The collimators consist of two jaws made of heavy material. They are placed between the beam and the vacuum chamber to collect beam halo particle or abnormal beam losses. The distance between the center of the beam and the surface of the collimator jaw is called collimator half-opening and depends on the type of collimator. Figure 6 shows a collimator that is installed in the LHC ring.

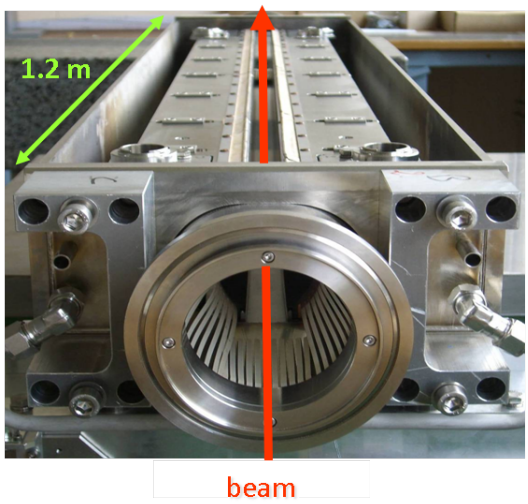

Figure 6: Photo of one collimator, placed between center of the beam and the vacuum chamber

All in all, 88 collimators are installed along the LHC ring as illustrated in Fig. 7. The figure shows that the collimators are installed on each side of the four main experiments ATLAS, ALICE, CMS and LHCb to prevent the detectors from large beam losses and to absorb luminosity debris from the IPs in IP1, IP2, IP5 and IP8. Several collimators are installed in the injection and extraction region to absorb beam losses during the injection process due to related failures.

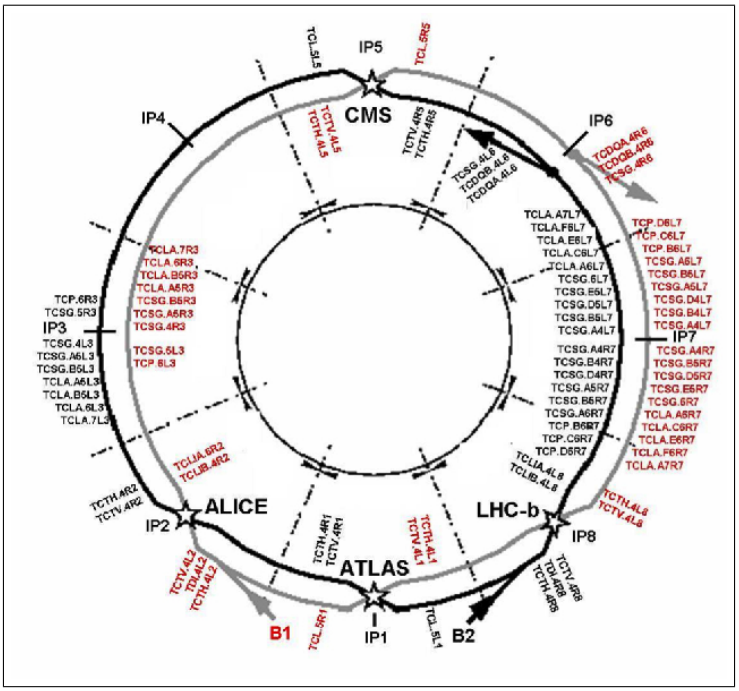

Figure 7: Locations of collimators in the LHC. Most collimators are located at the momentum and betatron cleaning in IR3 and IR7.

However, most of the collimators are located in the insertion region IR3 and IR7 where the beam cleaning takes place. The momentum cleaning in IR3 is the extraction of all particles with deviating momentum. In IR7 the betatron cleaning is performed. The collimators intercept all particles with large betatron amplitudes (betatron amplitude is explained in Sec. 4.2).
Since the collimators from that region become more important in that thesis, the layout of them is described in more detail.
The betatron cleaning region contains different types of collimators that ensure a multi-stage cleaning (see Fig. 8). These are primary collimators (TCP), secondary collimators (TCSG), tertiary collimators (TCT) and absorbers (TCLA). TCPs and TCSGA are made of fiber-reinforced copper to make them extremely robust and TCTs or TCLAs are made of a tungsten based material to absorb as much energy as possible[2].
Primary collimators, the closest elements to the beam, scatter the beam halo particles into the secondary halo that is intercept by the TCSG collimators, which half-opening is higher than for the TCPs. Most of the secondary particles are absorbed by the TCSG but they can also produce showers or tertiary halo particles by inelastic scattering that are intercept by absorbers or tertiary collimators. These multi-stage cleaning ensure an efficient interception of beam loss particles.

[2]High-Z materials like tungsten have a high efficiency for absorbing the energy but they are sensitive to beam damage. Therefore, tungsten collimators are only used to intercept secondary or tertiary particles at larger distance from the beam center [11].

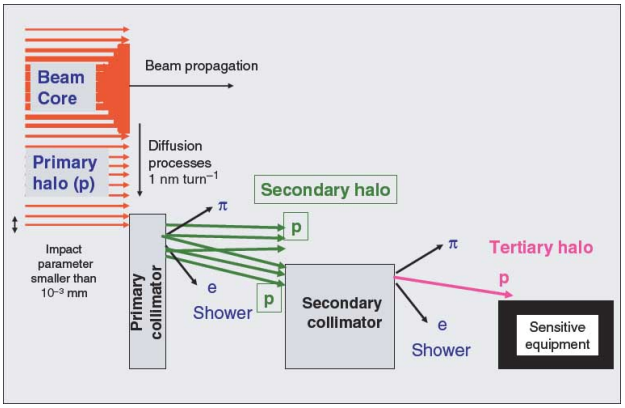

Figure 8: Layout of the multi-stage cleaning in the betatron cleaning insertion (taken from [1])

3.5 Ionization Chamber and Diamond Beam Loss Monitors

The previous sections explained the need for the observation and a monitoring of the beam losses. In case of high beam losses, the beam is dumped. Such a monitoring prevents superconducting magnets from quenching and protects LHC equipment from damage. Therefore, beam loss monitors are located at the superconducting magnets, collimators and in the injection and extraction regions. Additionally, a beam loss monitoring provides information about the beam loss mechanism and helps to identify the reason for a beam loss.

Two different systems are installed in the LHC to measure beam losses: ionization chambers and diamond detectors. Both system use ionization inside the gas or material to detect beam loss particles. If a charged particle is travelling through matter it is loosing energy by knocking electrons out of the material atoms along its path.

The energy loss due to ionization and also excitation is given by the Bethe-Bloch Formula [12]:

$$-\left(\frac{dE}{dx}\right) = Kz^2\frac{Z}{A}\frac{1}{\beta^2}\left[\frac{1}{2}ln\left(\frac{2m_ec^2\beta 2\gamma^2 T_{max}}{I^2}\right) - \beta^2 - \frac{\delta(\beta\gamma)}{2}\right], \tag{3.6}$$

where

$$\begin{aligned} K &= 4\pi N_A r_e^2 m_e c^2 \\ \beta &= \frac{v}{c} \\ \gamma &= \frac{1}{\sqrt{1-\beta^2}} \\ T_{max} &= \frac{2m_ec^2\beta^2\gamma^2}{1+2\gamma\frac{m_e}{m_0}+\left(\frac{m_e}{m_0}\right)^2}. \end{aligned}$$

The definition of the variables used in the Bethe Bloch formula are given in Table 1.

The energy loss for different materials is given in Fig. 9.

Variable	Definition
z	charge of incoming particle
Z	atomic number of material
A	atomic weight of material
m_e	mass of electron
m_0	mass of incoming particle
c	speed of light
T_{max}	maximum energy transfer
I	excitation potential of atoms in the material
N_A	Avogadros number
r_e	classical electron radius
δ	density correction factor

Table 1: Variables for Bethe Bloch formula.

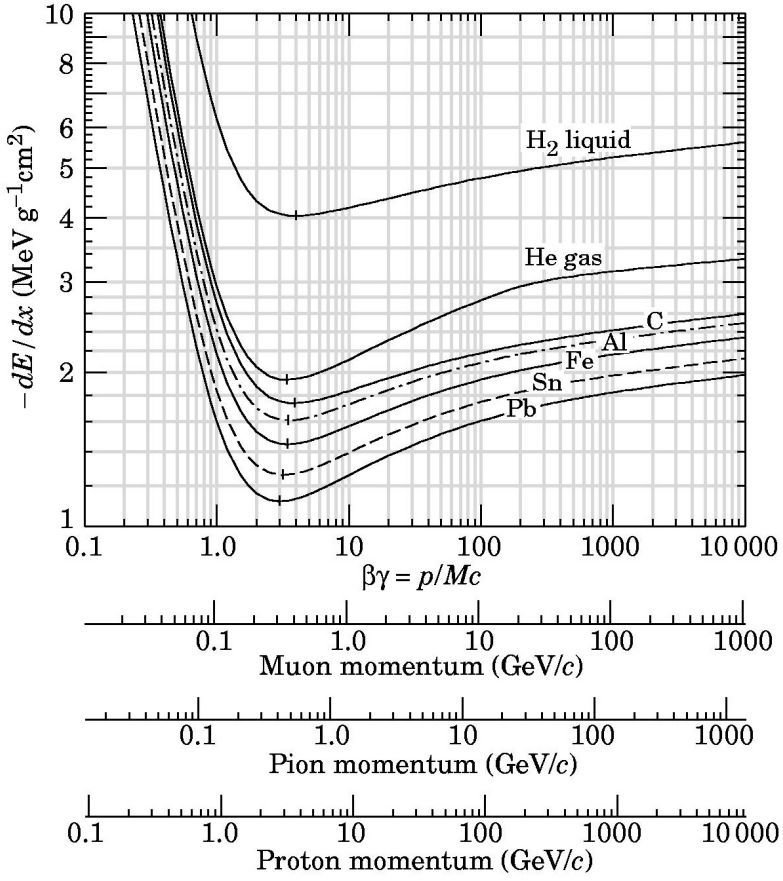

Figure 9: Energy loss for hydrogen, gaseous helium, carbon, aluminium, iron, tin and lead as a function of $\beta \cdot \gamma$.

The free charge carriers have to be separated to use an ionization chamber or diamond as a detector. That is done by an external electrical field that is generated by applying a high voltage. The drift of the free charge carriers can be measured as a current and the provided signal contains information about the number of the charged particles crossing the sensor and their arrival time. An illustration of a signal generation due to an ionization process is given in Fig. 10.

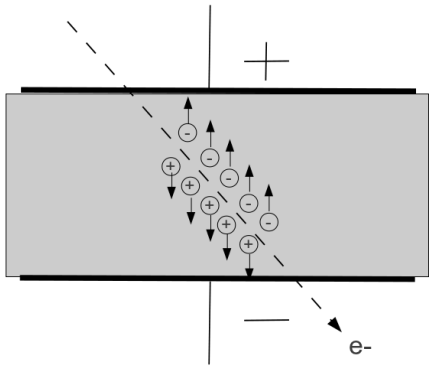

Figure 10: Signal generation due to ionization in a solid state detector. The charged particle creates electron-hole pairs along its trajectory which are separated by an applied electrical field and drift to teh respective electrode.

The signal generation for an ionization chamber and diamond detectors are due to ionization. The difference between them is that ionization chambers are filled with nitrogen gas and diamond is a solid state ionization chamber [13].

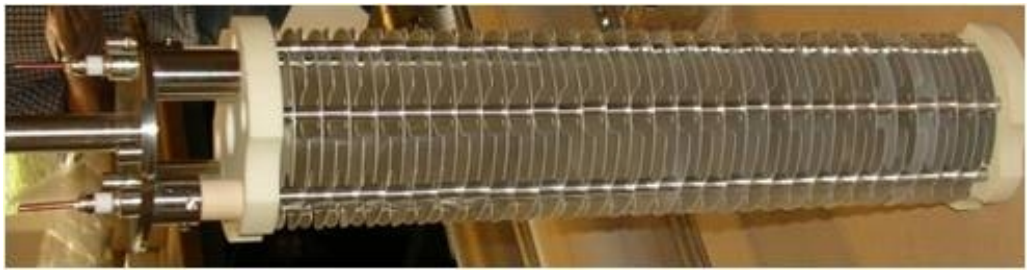

Figure 11: Photograph of the inside of an ionization chamber showing the aluminum electrodes.

Figure 11 shows an ionization chamber that is installed in the LHC. Ionization chambers are about 50 cm long and of 9 cm diameter. The standard ionization chambers used in the LHC contain several parallel aluminum electrodes that are separated by 0.5 cm and are filled with 1.5 l of N_2 at 100 mbar overpressure. Over 3600 ionization chambers measure beam losses with a dynamic range higher than 10^9 and a time resolution of 40 μs. Signals from ionization chambers are counted and integrated with 12 different time intervals (from 40 μs to 83.3 s). The beam losses of each integration time are compared to a table of thresholds. If the measured signal is above the threshold, a permit signal is removed and a beam dump follows.
Diamond detectors are not included in this protection system and cannot send a beam dump signal. Their tasks are the monitoring and observation of beam losses with a time resolution in the range of 1 ns. This time resolution allows a bunch-by-bunch resolution and analysis of losses and therefore a better understanding of the beam loss mechanism. The size of these sensors is in the order of centimeters or millimeters and differs for poly and single crystalline diamond detectors. An example of a sensors is given in Fig. 12. The diamond sensor on that picture is a single crystalline diamond with a volume of 4.7 mm $\times$ 4.7 mm $\times$ 0.5 mm.

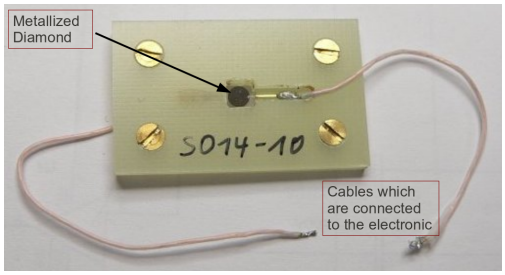

Figure 12: Photo of a diamond sensor with connectors for the readout electronic.

Several diamond detectors are located at regions with large beam losses as the betatron cleaning region or at the injection points. In addition, diamond detectors are placed near or inside the experiments (ATLAS, ALICE, CMS, LHCb). The diamond detectors provide valuable information about beam loss development, bunch pattern and also collision rates. All these measurements are analyzed in Sec. 8.

4 Linear Beam Optics

4.1 Derivation of Particle Equation of Motion in a Co-Moving Coordinate System

The equation of particle motion for particles is now derived following Ref. [6].
The trajectory of a particle circulating in a synchrotron is defined by the magnet structure and is called the design orbit. However, the magnets have always field errors and therefore the trajectory of the particle varies. The trajectory with magnetic field error is called closed orbit. The closed orbit is periodically and if an ideal particle would travel without error on the closed orbit, it would have the same trajectory for every revolution. However, particles in a beam have always an angular divergence and oscillate around the closed orbit. This oscillation is called betatron oscillation. We now need an equation of motion to describe the trajectory of a charged particle in a magnetic field of an accelerator.
To describe the motion of particles, we consider only the particles that move along the closed orbit with a small deviation. We assume again a particle movement in the horizontal plane as in Sec. 3.3. The Cartesian coordinate system is defined as $\overrightarrow{K} = (x, z, s)$ and moves along the closed orbit [6]. We assume that the particle moves parallel to the s-direction of the orbit with the velocity $\overrightarrow{v} = (0, 0, v_s)$ as illustrated in Fig. 13.

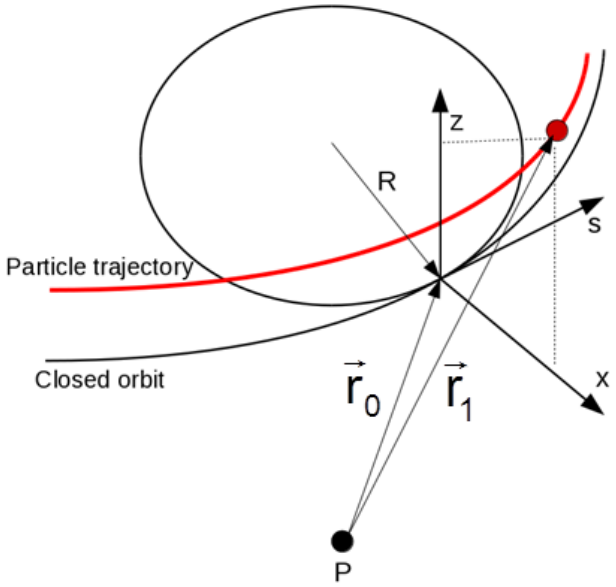

Figure 13: Rotated coordinate system to describe the particle movement.

The coordinate system is fixed in the x-s plane on the closed orbit.
The particle is now deflected by a magnet with the bending radius R and the system rotates therefore from $\overrightarrow{x_0}$ and $\overrightarrow{s_0}$ to $\overrightarrow{x}_1$ and $\overrightarrow{s_1}$. The vectors $\overrightarrow{x_0}$ and $\overrightarrow{s_0}$ have to be transformed to the new

coordinates with the rotation angle φ (azimuth angle of the polar coordinates):

$$\begin{aligned} \overrightarrow{x_1} &= \overrightarrow{x_0}\cos\varphi + \overrightarrow{s_0}\sin\varphi \\ \overrightarrow{s_1} &= -\overrightarrow{x_0}\sin\varphi + \overrightarrow{s_0}\cos\varphi \ . \end{aligned}$$

After a differentiation of these vectors it follows that

$$\begin{aligned} \frac{d\overrightarrow{s_0}}{d\varphi} &= -\overrightarrow{x_0} \\ \frac{d\overrightarrow{x_0}}{d\varphi} &= \overrightarrow{s_0} \ . \end{aligned}$$

With the usage of the path element of a curved trajectory, which is defined as $ds = Rd\varphi$, the time derivative becomes:

$$\begin{aligned} \dot{\overrightarrow{x_1}} &= \frac{d\overrightarrow{x_1}}{d\varphi}\frac{d\varphi}{dt} = \frac{1}{R}\dot{s}\overrightarrow{s_1} \\ \dot{\overrightarrow{s_1}} &= \frac{d\overrightarrow{s_1}}{d\varphi}\frac{d\varphi}{dt} = -\frac{1}{R}\dot{s}\overrightarrow{x_1} \\ \dot{\overrightarrow{z_1}} &= 0 \ . \end{aligned} \tag{4.1}$$

Since the coordinate system moves along the closed orbit by $d\overrightarrow{r_1} = \overrightarrow{s_1}ds$ the time derivative of $\overrightarrow{r_1}$ is $\dot{\overrightarrow{r_1}} = \dot{s}\overrightarrow{s_1}$. The position of the particle is now given by $\overrightarrow{r}$ which can be written as $\overrightarrow{r} = \overrightarrow{r_1} + x\overrightarrow{x_1} + z\overrightarrow{z_1}$. The variable x and z are then the deviations of the closed orbit as illustrated in Fig. 14.

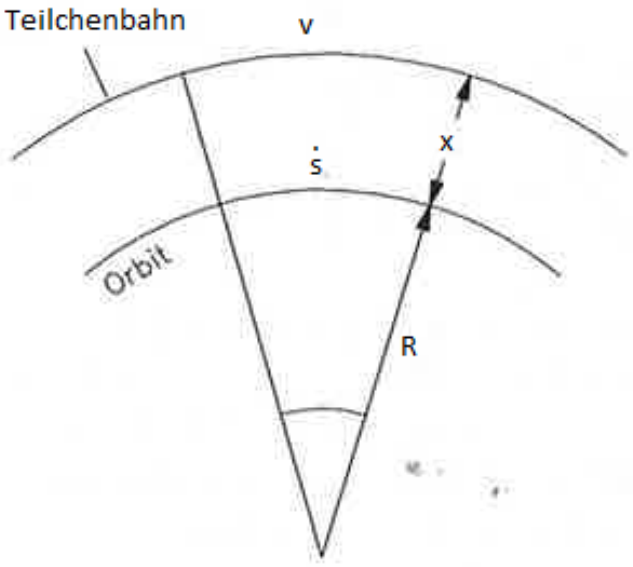

Figure 14: Illustration of the difference between orbit and particle trajectory where x is the deviation of the particle from the orbit, v the particle velocity and $\dot{s}$ the velocity of the coordinate system (taken from [6]).

Later we need the first and second time derivatives of the position vector $\overrightarrow{r}$ that follow from Eq. (4.1):

$$\dot{\overrightarrow{r}} = \dot{x}\overrightarrow{x_1} + \dot{z}\overrightarrow{z_1} + \left(1 + \frac{x}{R}\right)\dot{s}\overrightarrow{s_1} \tag{4.2}$$

$$\ddot{\overrightarrow{r}} = \left[\ddot{x} - \left(1 + \frac{x}{R}\right)\frac{\dot{s}^2}{R}\right]\overrightarrow{x_1} + \ddot{z}\overrightarrow{z_1} + \left[\frac{2}{R}\dot{x}\dot{s} + \left(1 + \frac{x}{R}\right)\ddot{s}\right]\overrightarrow{s_1} \tag{4.3}$$

We can write now the time derivative of $\dot{x}$ and $\ddot{x}$ as a time derivative of s since the position s of the particle is known at any time.

$$\begin{aligned} \dot{x} &= \frac{dx}{ds}\frac{ds}{dt} = x'\dot{s} \\ \ddot{x} &= x''\dot{s}^2 + x'\ddot{s} \end{aligned} \tag{4.4}$$

With Eq. (4.3) we then get:

$$\begin{aligned} \dot{\overrightarrow{r}} &= x'\dot{s}\overrightarrow{x_1} + z'\dot{s}\overrightarrow{z_1} + \left(1 + \frac{x}{R}\right)\dot{s}\overrightarrow{s_1} \\ \ddot{\overrightarrow{r}} &= \left[x''\dot{s}^2 + x'\ddot{s} - \left(1 + \frac{x}{R}\right)\frac{\dot{s}^2}{R}\right]\overrightarrow{x_1} + \ddot{z}\overrightarrow{z_1} + \left[\frac{2}{R}\dot{x}\dot{s} + \left(1 + \frac{x}{R}\right)\ddot{s}\right]\overrightarrow{s_1} \end{aligned} \tag{4.5}$$

These expressions describe the motion of the particle related to the closed orbit but without the influence of the magnetic field. The charged particle with the charge q and the mass m is deflected by the Lorenz force of the magnetic field in an accelerator that can be written as:

$$F_L = m\ddot{r} = q\left(\dot{\overrightarrow{r}} \times \overrightarrow{B}\right) . \tag{4.6}$$

The magnetic field is defined only in the x- and z-directions $\overrightarrow{B} = (B_x, B_z, 0)$ (see Sec. 3.3) and therefore the vector product of $\overrightarrow{r}$ and $\overrightarrow{B}$ leads to the expression

$$\ddot{r} = \frac{q}{m}\begin{pmatrix} -\left(1 + \frac{x}{R}\right)\dot{s}B_z \\ \left(1 + \frac{x}{R}\right)\dot{s}B_x \\ x'\dot{s}B_z - z'\dot{s}B_x \end{pmatrix} . \tag{4.7}$$

Equation (4.7) shows the influence of the magnet field on the particle in each direction. However, if the charged particle travels with speed of light, the influence on the longitudinal component s is negligible. The x and z components can be written as

$$\begin{aligned} x''\dot{s}^2 + x'\ddot{s} - \left(1 + \frac{x}{R}\right)\frac{\dot{s}^2}{R} &= -\frac{q}{m}B_z\left(1 + \frac{x}{R}\right)\dot{s} \\ z''\dot{s}^2 + z'\ddot{s} &= \frac{q}{m}B_x\left(1 + \frac{x}{R}\right)\dot{s} \end{aligned} \tag{4.8}$$

using Eq. (4.5). We can assume that the velocity of the particle changes slowly and set $\ddot{s} \approx 0$. The mass can be expressed by the momentum $p = mv$ and the velocity is $v = \dot{s}\,(1 + x/R)$ (given by the geometry of Fig. 14). The new expressions are:

$$\begin{aligned} x'' - \left(1 + \frac{x}{R}\right)\frac{1}{R} &= -\frac{q}{p}B_z\left(1 + \frac{x}{R}\right)^2 \\ z'' &= \frac{q}{p}B_x\left(1 + \frac{x}{R}\right) \end{aligned} \tag{4.9}$$

The magnetic field for B_x and B_z is already explained in Sec. 3.3 Eq. (3.4). However, we only take the dipole and quadrupole terms which is defined as the linear beam optics. Additionally, the deflection of the dipole is only in the x-direction. With these information we can write B_x and B_z as

$$\begin{aligned} \frac{q}{p}B_z &= \frac{1}{R} - kx \\ \frac{q}{p}B_x &= -kz \ , \end{aligned} \tag{4.10}$$

where k is the quadrupole strength. The momentum of the particle is $p = p_0 + \Delta p$, where Δp is a small deviation from the nominal momentum p_0. With the usage of the relative momentum deviation $\Delta p/p$ we get to first order

$$\begin{aligned} x'' - \left(1 + \frac{x}{R}\right)\frac{1}{R} &= -\left(1 + \frac{x}{R}\right)^2\left(\frac{1}{R} - kx\right) = \left(1 - \frac{\Delta p}{p}\right) \\ z'' &= -\left(1 + \frac{x}{R}\right)^2 kz\left(1 - \frac{\Delta p}{p}\right) \ . \end{aligned} \tag{4.11}$$

At the end we can multiply out the brackets and assume that the deviation of the particle is very small compared to the radius R which means that squares of x and z and also xz are ≈ 0. The final equation of motion of a charged particle through a magnetic structure is then

$$x''(s) + \left(\frac{1}{R^2(s)} - k(s)\right)x(s) = \frac{1}{R(s)}\frac{\Delta p}{p} \tag{4.12}$$

$$z''(s) + k(s)\,z(s) = 0 \ . \tag{4.13}$$

Equation (4.12) and (4.13) are the basics of the calculations of the particle trajectories in accelerator physics [6] and are used for the next section.

4.2 Beta Function and Betatron Oscillation

The derived equations from the previous section describe a charged particle that travels trough the magnetic structure of an accelerator with a small variation from its momentum Δp around the nominal value. They contain the assumption that only the trajectory of one single particle is bent by the magnets. However, one bunch in the LHC consists of $1.15 \cdot 10^{11}$ protons which we want to describe, too.

To do so we can take again the basic equation of motion from Eq. (4.12) and simplify them. We assume that $1/R = 0$ and the relative momentum deviation is $\Delta p/p = 0$. The equation becomes

$$x''(s) - k(s) = 0 \; . \tag{4.14}$$

The quadrupole strength k is known at each position s in the LHC ring.
The solution of this differential equation is a transverse oscillation

$$x(s) = Au(s)\cos(\Psi(s) + \phi) \; , \tag{4.15}$$

where $Au(s)$ is the amplitude of the oscillation, $\Psi(s)$ the phase depending on the location s and ϕ the constant phase of the oscillation. In the case of a small angular divergence, that cannot be avoided within the beam, the particle oscillates around the closed orbit with the amplitude $Au(s)$ and the phase $\Psi(s)$. The factor A in Eq. (4.15) is a constant and defined as

$$A := \sqrt{\epsilon} \; , \tag{4.16}$$

where ϵ is the emittance. A small emittance corresponds to a small beam size.
Equation (4.15) specifies the deviation related to the closed orbit at each position s in the ring. The amplitude function $u(s)$ depends on the position s due to the magnetic structure and it is defined as:

$$\beta(s) = u^2(s) \; . \tag{4.17}$$

Equation (4.17) is an expression for the amplitude function of an particle with an oscillation and $\beta(s)$ is called beta function which is given by the LHC magnet structure. The beta function depends on the beam focussing and varies with the position. Also the phase of the oscillation depends on the position and it can be written with the definition of the betatron amplitude as:

$$\Psi(s) := \int_0^s \frac{d\bar{s}}{u^2}(\bar{s}) = \int_0^s \frac{d\bar{s}}{\beta(\bar{s})} \; , \tag{4.18}$$

where $\Psi(s)$ is the phase of the oscillated particle at a certain position.
For a system with many particles, the envelope of the betatron oscillation of all particles becomes more important as illustrated in Fig. 15.
It shows the betatron oscillation $x(s)$ for one and for many particles. All trajectories of the particles are inside the envelope that defines therefore the beam size. The envelope is defined as

$$E(s) := \sqrt{\epsilon\beta(s)} \; . \tag{4.19}$$

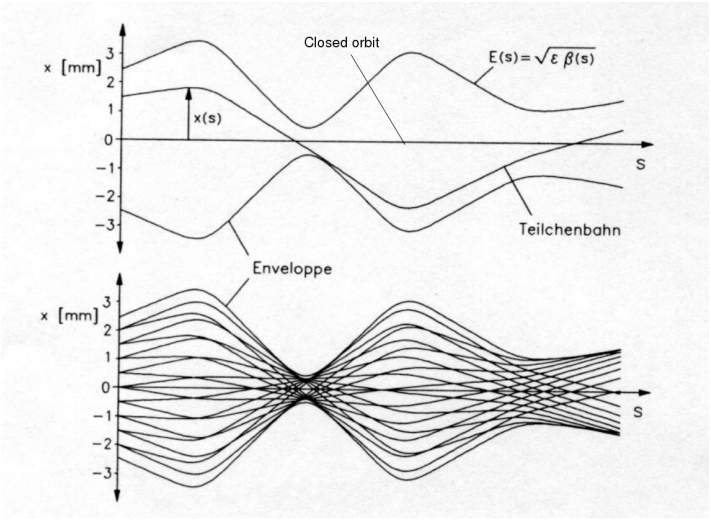

Figure 15: Illustration of betatron oscillation and enevelope (taken from [6]).

With the definition of the beta function and the emittance the betatron oscillation and the first derivative of x become:

$$x(s) = \sqrt{\epsilon}\sqrt{\beta(s)}\cos(\Psi(s)+\phi) \tag{4.20}$$

$$x'(s) = -\frac{\sqrt{\epsilon}}{\sqrt{\beta(s)}}\left[-\frac{\beta'(s)}{2}\cos(\Psi(s)+\phi)+\sin(\Psi(s)+\phi)\right] , \tag{4.21}$$

where x is the radial deviation of the particle from the closed orbit and x' is the radial angle deviation.
Note that these equations are valid for the vertical and horizontal planes since we assumed that $1/R = 0$.
All particles make several betatron oscillation in one complete revolution around the LHC ring and the number of betatron oscillation in one turn is called tune Q.
At the beginning of this chapter it is explained that the closed orbit is periodically and that particle follows the same trajectory over and over again. However, that is not valid anymore for particles that are not on the closed orbit. The tune is a non-integer, therefore, the phase ϕ is different at each turn. The tune in the LHC x-plane is $Q_x = 59.31$ with a fractional tune of ~ 0.31.
Particles with a change in the momentum $\Delta p/p$ have also a different tune

$$\frac{\Delta Q}{Q} = \xi\frac{\Delta p}{p} , \tag{4.22}$$

where ξ is the chromaticity.

4.3 Transfer Matrix

The topic now is to track particles along the accelerator and get information about the deviation x and the angle x' of the particle after it travels trough a magnetic structure.

To get these informations, we need a transfer matrix of the form

$$\begin{pmatrix} x(s) \\ x'(s) \end{pmatrix} = \mathbf{M} \begin{pmatrix} x_0 \\ x'_0 \end{pmatrix} , \tag{4.23}$$

where x_0 and x'_0 are the start parameter and $x(s)$ and $x'(s)$ are the parameters after the magnet structure. To get the matrix $\mathbf{M}$ we take the Eq. (4.20) and (4.21) and use the rules of addition of trigonometric functions. It reads:

$$x(s) = \sqrt{\epsilon}\sqrt{\beta(s)}\left[\cos\Psi(s)\cos\phi - \sin\Psi(s)\sin\phi\right] \tag{4.24}$$

$$x'(s) = -\frac{\sqrt{\epsilon}}{\sqrt{\beta(s)}}\Big[\alpha(s)\cos\Psi(s)\cos\phi - \alpha(s)\sin\Psi(s)\sin\phi + \sin\Psi(s)\cos\phi + \cos\Psi(s)\sin\phi\Big] , \tag{4.25}$$

where

$$\alpha(s) = \beta'(s)/2 . \tag{4.26}$$

With the initial condition of $x(0) = x_0$, $x'(0) = x'_0$, $\beta(0) = \beta_0$ and $\alpha(0) = \alpha_0$ it follows that

$$\cos\phi = \frac{x_0}{\sqrt{\epsilon\beta_0}} \tag{4.27}$$

$$\sin\phi = -\frac{1}{\sqrt{\epsilon}}\left(x'_0\sqrt{\beta_0} + \frac{\alpha_0 x_0}{\sqrt{\beta_0}}\right) . \tag{4.28}$$

The expression for $\sin\phi$ and $\cos\phi$ can be inserted in Eq. (4.24) and (4.25) and x and x' become

$$x(s) = \sqrt{\frac{\beta(s)}{\beta_0}}\left[\cos\Psi(s) + \alpha_0\sin\Psi(s)\right]x_0 + \sqrt{\beta(s)\,\beta_0}\sin\Psi(s)x'_0 \tag{4.29}$$

$$x'(s) = \frac{1}{\beta(s)\,\beta_0}\left[(\alpha_0 - \alpha(s))\cos\Psi(s) - (1 + \alpha_0\alpha(s))\sin\Psi(s)\right]x_0 + \sqrt{\frac{\beta_0}{\beta(s)}}\left[\cos\Psi(s) - \alpha(s)\sin\Psi(s)\right]x'_0 . \tag{4.30}$$

From Eq. (4.29) and (4.30) we can directly get the matrix $\mathbf{M}$ which is then

$$\mathbf{M} = \begin{pmatrix} \sqrt{\frac{\beta}{\beta_0}}\left(\cos\Psi + \alpha_0\sin\Psi\right) & \sqrt{\beta\beta_0}\sin\Psi \\ \frac{(\alpha_0-\alpha)\cos\Psi - (1+\alpha_0\alpha)\sin\Psi}{\beta\beta_0} & \sqrt{\frac{\beta_0}{\beta}}\left(\cos\Psi - \alpha\sin\Psi\right) \end{pmatrix} . \tag{4.31}$$

Notice that Ψ is the phase advance between the starting and end point of the trajectory:

$$\Psi = \Psi(s_2) - (s_1) . \tag{4.32}$$

With that matrix we can calculate the position and angle between two different positions in the LHC ring. Additionally, it is also possible to calculate the deviation of a particle that got a change

in angle due to a scattering process with dust or gas particles. An example for such a scenario is given in the following.
We assume a proton on the closed orbit with $x_0 = 0$ and $x_0' = 0$ that is elastically scattered by a residual gas particle. The angle changes due to the scattering process by for example $50 \mu rad$ and the angle x_0' becomes $x_0' = 0 + 50\,\mu\text{rad}$. We also assume that the scattering process happens in the x-plane and in one of the kicker magnets that is called MKI.D5L2.B1. The beta function and the phase at the kicker magnet are $\beta_0 = 158.39\,\text{m}$ and $\Psi_{MKI} = 7.84 \cdot 2\pi$ (the phase advance is given in units of 2π). We can now get the information about the deviation $x(s)$ at a collimator in IR3 called TCP.6L3.B1 where the beta function and phase are $\beta = 131.52\,\text{m}$ and $\Psi_{TCP} = 16.10 \cdot 2\pi$. The deviation x at the collimator can be calculated with Eq. (4.23):

$$\begin{aligned} x(s_{TCP}) &= \sqrt{\beta\beta_0}\sin(\Psi_{TCP} - \Psi_{MKI})x_0' \\ &= 7.178\,\text{mm} \end{aligned} \tag{4.33}$$

Since the TCP collimator has an half opening gap of 4.2 mm, the proton hits the collimator and is lost. Equation (4.33) shows that the maximum orbit deviation is reached at positions with $\sin\Psi = 1$. It also illustrates that the deviation of a single turn trajectory is proportional to the angle kick x_0'. The smaller the kick the smaller the deviation. It could happen that a proton on the closed orbit, scattered by a particle, is not captured by the collimators because the kick is not large enough and the maximum deviation is smaller than the opening gap. Another case is that the proton may not hit the collimator in the first turn even though the maximum amplitude is larger than the opening gap because the maximum amplitude depends also on the phase advance as illustrated in Fig. 16.

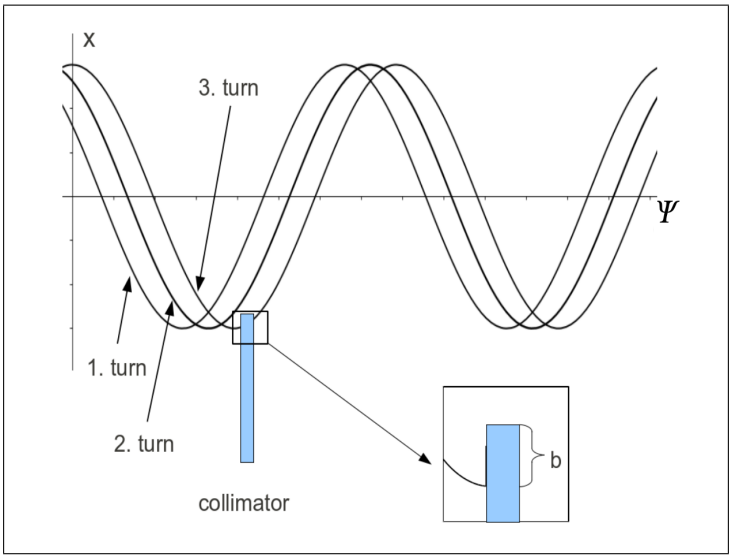

Figure 16: Definition of impact parameter b and the relation between the deviation x and the phase advance Ψ for a tune of ~ 0.1.

This Figure shows that the proton hits the collimator after the third turn due to the change of the phase after each turn due to the fractional tune of 0.3 . The variable b in the figure is the impact

parameter that is defined as the distance between inner edge of the collimator and the point where the proton hits the collimator. To summarize, it depends on both the size of the angle kick and the phase advance if a particle is lost after a scattering process or not. It is possible that a particle is not intercepted by the collimators after the first turn but after several turns.

5 Beam Losses Caused by Dust Particles

One important beam loss process is the scattering of a proton from the LHC bunches by a dust or residual gas particle. In the former case it is also called UFO (Unidentified Falling Object) because the origin of such an event is still under investigation. It is believed that dust particles in the micrometer range fall from above into the beam which leads to a scattering of many protons and to beam losses in each bunch that is circulating in the LHC within 10 turns [14].
Beam losses due to scattering processes can be registered by diamond detectors or ionization chambers. The beam loss profile of UFO events over the time measured with an ionization chamber is typically Gaussian as shown in Fig. 17. Many UFO measurements from ionization chambers were taken with a time resolution of 40 μs (a half LHC turn). The information about beam losses per bunch is therefore not possible.

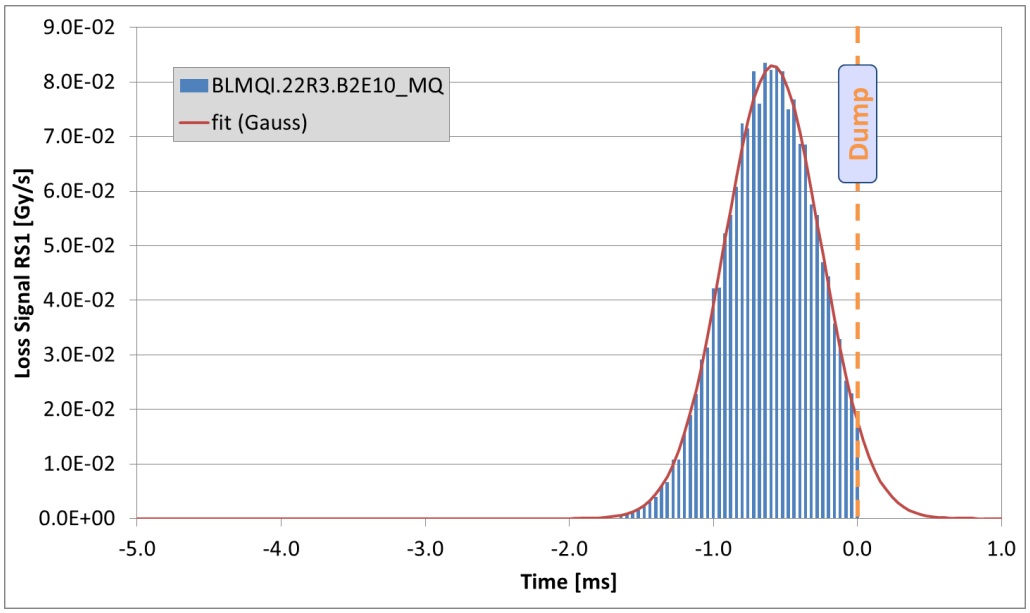

Figure 17: A typically UFO measurement from one ionization chambers in IR3 [14]. The loss profile for UFO events is Gaussian. The beam was dumped due to large beam losses.

UFOs can occur everywhere around the LHC ring as shown is Fig. 18 but with maximum occurrence in the kicker magnets (MKI) in IR2 and IR8.
The vacuum chambers are made of ceramic (Al_2O_3). A X-ray spectroscopy of the particles in the ceramic chambers detected many of Al_2O_3 particles which can fall into the proton beam due to vibrations during the injection process (see Sec. 3.2). FLUKA[3] simulations with scattering of protons on aluminum nuclei explain this observation [17]. The results of the scattering dynamics, including the recoil of the dust particle, are given in Ref. [18].

[3]FLUKA is a general purpose tool for calculations of particle transport and interactions with matter. It simulates, based on Monte Carlo techniques, scattering processes in a proton or electron accelerator [15, 16].

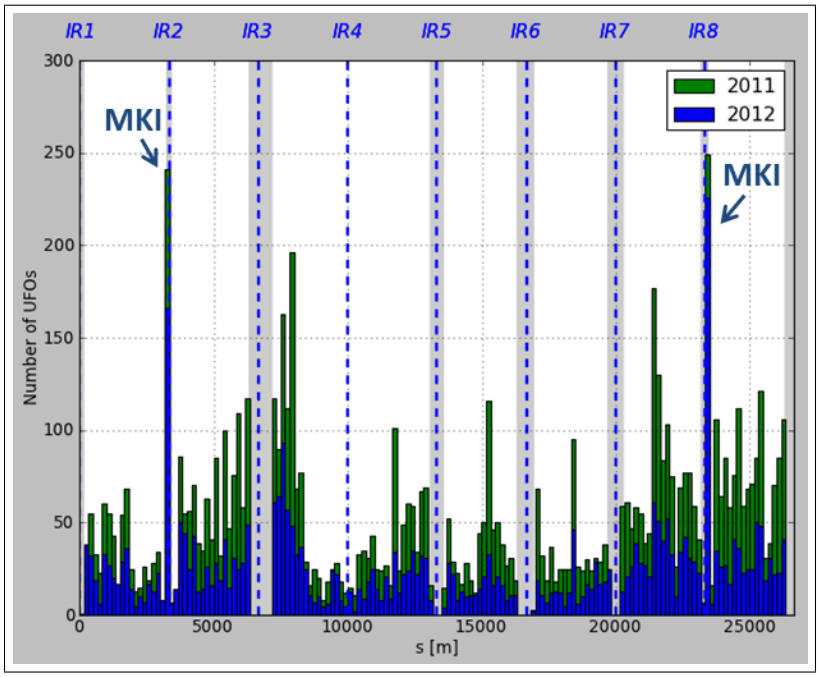

Figure 18: Locations of UFO events around the LHC ring [19]. Most of the UFO events occur at the injection region in IR2 and IR8, marked with "MKI".

6 Simulations with MadX

6.1 Scattering Processes of Protons

In order to understand beam losses caused by UFO events it is necessary to understand the interaction between protons and nuclei of the dust particle.
Interaction of protons with nuclei can be classified in elastic and inelastic scattering. The inelastic scattering of a proton p and a nuclus N generates many particles at relatively large angle. That leads to localized beam losses due to the collision products $a, b, c, ...$:

$$p + N \quad \rightarrow \quad a + b + c + \dots \ . \tag{6.1}$$

The collision products have a different charge/mass ratio and they are therefore not able to stay in the LHC acceptance. After an inelastic scattering, the proton is lost.
In the case of an elastic scattering the proton p still exists after it is scattered by a nuclei N:

$$p + N \quad \rightarrow \quad p + N \ . \tag{6.2}$$

Only a transfer of momentum takes place which can be described by

$$\overrightarrow{q} \quad = \quad \overrightarrow{p_i} - \overrightarrow{p_d} \ , \tag{6.3}$$

where $\overrightarrow{q}$ is the 4-momentum transfer, $\overrightarrow{p_i}$ the incoming momentum and $\overrightarrow{p_d}$ the outgoing momentum of the proton. We can assume that the absolute values of the incoming and outgoing momentum are about the same $p = |p_i| = |p_d|$ in case of a heavy nucleus as a scattering particle. The momentum transfer causes a deflection of the proton with the scattering angle Θ and can be calculated with the help of Eq. (6.3) and the absolute value of both momenta:

$$\overrightarrow{q}^2 \quad = \quad 4p^2 \sin^2 \frac{\Theta}{2} \ . \tag{6.4}$$

For elastic scattering between protons and a heavy nuclus, the distribution of the scattering angle is a Gaussian,

$$P\left(\Theta\right) \quad = \quad c \cdot \exp^{-10.2\,\mathrm{GeV}^{-2} A^{3/2} p^2 \Theta^2} \ , \tag{6.5}$$

where A is the number of nucleons in the nucleus and c a normalization constant [20]. Since UFOs are much heavier than protons Eq. (6.5) is a good approximation. The proton, which is deflected by the angle Θ, can hit the collimators after some turns and is lost.

6.2 Transport of Protons in the LHC Ring

This section concentrates on elastic scattering since the beam losses due to an elastic scattering event can be detected over several turns by the loss monitors and especially in the cleaning region (IR7). The idea is to detect beam losses in IR7 even though the event occured anywhere in the LHC ring.

With FLUKA elastic scattering is simulated and the four momenta of the scattered particle is given. A tracking program for the whole LHC is required to get information about the location of beam losses along the LHC ring.
A program for that purpose is MadX. MadX describes particle accelerators, their beam optics and simulates the beam dynamics. It calculates the trajectory of particles influenced by the magnets. Additionally, the collimator settings are loaded in MadX and if the amplitude of betatron oscillation of a proton is higher than the opening gap of the collimator, the proton is lost. Therefore, it gives information about the position where a proton is lost. Note that the collimators in MadX are black absorbers. If a proton crosses such a black absorber, it is lost and does not produce secondary particles.
The beam losses due to an UFO[4] in the kicker magnet in IR2 were simulated in two steps. First, an elastic scattering process was simulated by FLUKA[5] providing the angular distribution. The second step is the MadX simulation which takes the angular distribution as an input. It calculates the betatron oscillation of each proton due to the anglular deviation x' (see Sec. 4.2) and provides the information if a proton hits a collimator. MadX tracks also the proton over several turns to take into account that a particle may not hit the collimator in the first turn. At the end a distribution of locations, where the protons are lost, is created.
The simulation was done with $600,000$ elastically scattered protons with a tracking over 10 LHC turns to reconstruct the beam losses of an UFO event in the kicker magnet MKI.D5L2.B1. The distribution of the proton loss is given in Fig. 19. The kicker magnet MKI.D2L2.B1 is left of IP2 and the UFO event occurred in beam 1 that is circulating anticlockwise around the LHC ring.

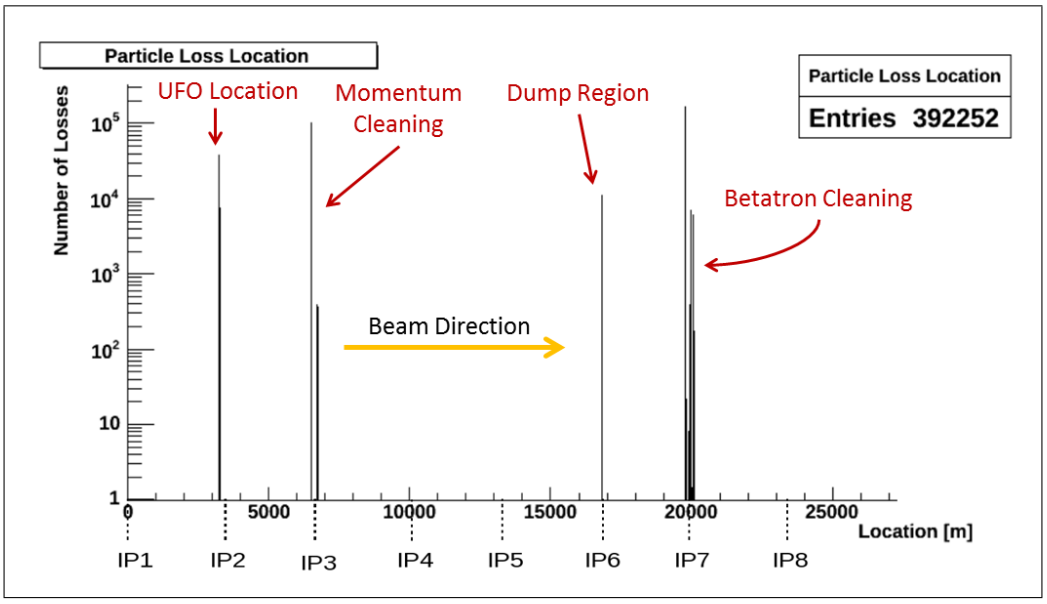

Figure 19: Distribution of particle losses around LHC over 10 turns. Most losses are observed at the cleaning region in IR7 on both sides of the IP7.

The plot shows several positions of beam losses: IR2, in IR3, in IR6 and IR7.
Two different collimators are located in the IR2 region, one collimator for the horizontal plane

[4] A point-shaped aluminum particle was assumed.
[5] The simulation was done by Anton Lechner CERN EN-STI and the FLUKA team.

and another one for the vertical plane. Since the opening gap in IR2 is very large (opening gap in IR2 is $15\,\sigma$)[6], only protons with a large betatron amplitude are lost in the vertical and horizontal planes. These protons are intercepted by the collimators in IR2 directly after the scattering process because of a large scattering angle.
Collimators in IR3 are closer to the beam than in IR2 (opening gap in IR3 is $12\,\sigma$). Additionally, the phase advance between kicker magnet and collimators in IR3 is 90° ($\sin\Psi = 1$) in the horizontal plane. Therefore, the protons have a maximum orbit deviation in the horizontal plane in IR3. All the protons that have a horizontal amplitude higher than the opening gap in IR3 but smaller than in IR2 hit the collimators in IR3 and are lost in the horizontal plane in the first turn after the scattering process.
The most important collimation regions are IR6 and IR7 because there the collimators are nearest to the beam. The opening gap in the horizontal plane of the collimators in IR6 is $9.3\,\sigma$ and in IR7 $5.7\,\sigma$. The collimators in IR7 define the global aperture limit. If a scattered proton passes the previous collimators then it hits the collimators in IR6 and IR7. Most protons are lost in IR6 and IR7 in the horizontal plane.
Additionally, the beam losses in IR7 can be explained by the phase advance. It is explained in the previous section that protons may stay in the LHC acceptance over more than one turn even though the maximum amplitude of the betatron oscillation is larger than the half-opening gap for the collimators in IR7 but the amplitude for a certain phase is smaller than the half-opening gap. However, the fractional tune in the LHC is 0.3 and therefore the phase advance increases after each turn by $0.3 \cdot 2\pi$. Due to the change of the phase advance the amplitude of the betatron oscillation at a certain phase changes (see Sec. 4.3). The proton is captured by collimators after several LHC turns. Calculations of the horizontal phase advance between the kicker magnet in IR2 and the primary collimators in IR7 show that the trajectory deviation of the particles has a maximum for the 1st ($\Psi_1 = 122°$) and 4th ($\Psi_4 = 64°$) turn for a fractional tune of 0.28 (an illustration of the trajectory deviation for different turns is given in Fig. 20). Larger losses at this collimator are expected in the 1^{st} and 4^{th} turn.
The simulation shows that the collimators in IR7 are important because beam losses at that location can be observed during several turns. Even small beam losses can be detected due to the aperture limit and the phase advance in the LHC ring. The potential of the beam loss measurements in IR7 is exploited in Sec. 8.1.

[6]Sigma denotes the width of a Gaussian particle distribution in a bunch with a nominal normalized emittance of $3.5\,\mu$rad. The emittance of the beams for operation in 2012 is in the order of 2-2.5 μrad.

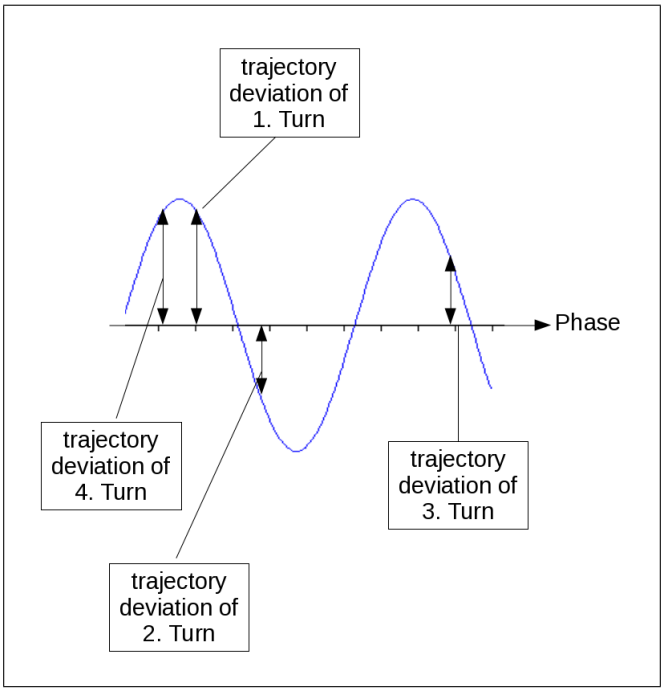

Figure 20: Trajectory deviation for 1^{st}, 2^{nd}, 3^{rd} and 4^{th} turn for the phase advance between kicker magnet in IR2 and primary collimator in IR7.

7 Diamond Detectors

7.1 Specification of Diamond Sensors

Diamond detectors became very attractive in the field of particle accelerators for various reasons. Diamond is a radiation-hard material and therefore it can be used in regions with a high radiation dose. Additionally, diamond detectors have very small leakage current with a negligible temperature dependence which makes them interesting for the LHC and their experiments like CMS. Inside CMS cooling is difficult due to limited space and monitoring of the beam condition with a detector without temperature dependence is needed. Also important is that the diamond sensors have a response time in the nanosecond range. That allows beam monitoring on a bunch-by-bunch basis. Bunch-by-bunch beam loss measurements are crucial to understand the beam loss processes.
The most common method to create clean diamond material is the chemical vapor deposition (CVD). It is based on the deposition of atomic carbon onto a substrate within a gaseous atmosphere. The CVD process allows to grow polycrystalline (pCVD) and single crystalline (sCVD) diamond. The polycrystalline diamond is much cheaper because it is easier to produce. The substrate for the pCVD process can be silicon or tungsten because they have similar lattice parameters as diamond. The pCVD diamond grows in a random orientation with a wafer size in the order of cm. The sCVD diamonds are more expensive since they can only grow on a single crystal diamond. Their typical size is in the mm range. Both pCVD and sCVD diamonds can be applied for particle detection but sCVD diamonds have a better energy resolution and better charge collection properties [21]. Both types of diamond detectors are installed in the LHC but with different readout and analysis systems. The different systems are explained in Sec. 7.2 and Sec. 7.3.
Diamond is due to its lattice the hardest natural material that is known. Each carbon atom has four bonds to neighboring atoms, resulting in a tetrahedron [22]. The diamond cubic lattice, that is illustrated in Fig. 21, is formed by bonding the neighboring carbon atom by sp^3 hybrid orbitals.

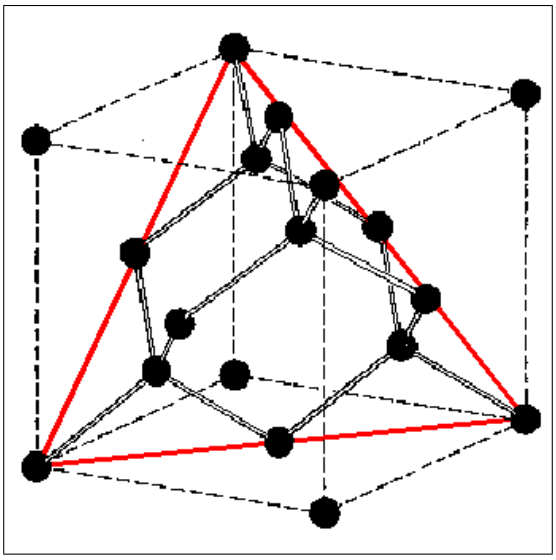

Figure 21: Schematic view of the diamond lattice (taken from http://biointerface.org).

In terms of electric properties, diamond is an insulator with a large band gap of 5.45 eV which leads to a very high resistivity of around $10^{13} - 10^{16}\,\Omega$cm. Due to the high resistivity the leakage current

at room temperature is very low (in the order of pA) and cooling or temperature stabilisation of diamond sensors is not needed. Diamond detectors have a low noise level and the performance is temperature independent.
In order to use diamond as a sensors it is needed to metallize the diamond surface and to apply high voltage to create a homogeneous electrical field inside the diamond bulk material. The resulting capacity is an important parameter and it is defined by the geometry and the dielectric constant ϵ_r :

$$C = \epsilon_0 \epsilon_r \frac{A}{d} , \tag{7.1}$$

where ϵ_0 is the absolute permittivity, A the area of the diamond and d the thickness. The dielectric constant for diamond is around 5.7 .
The signal generation in diamonds is described in Sec. 3.5. When a high energy charged particle passes through the diamond, it deposits part of its energy in the diamond by ionizing the diamond atoms. The electron-hole pairs are separated due to an external electrical field that is applied by electrodes bonded on the metalized surface. The electrons and holes drift to the oppositely charged electrode and generate a signal.
If the electrical field is not sufficiently high, the electron-hole pairs can recombine in the diamond and they do not contribute to the signal generation. The signal is proportional in that regime to the number of separated electron-hole pairs. Electrons emitted from a Sr-90 source β-decay were used to form a beam crossing the diamond and generate a signal. Figure 22 shows the diamond signal size as a function of the applied voltage. Such measurements are done to characterize diamond sensors.

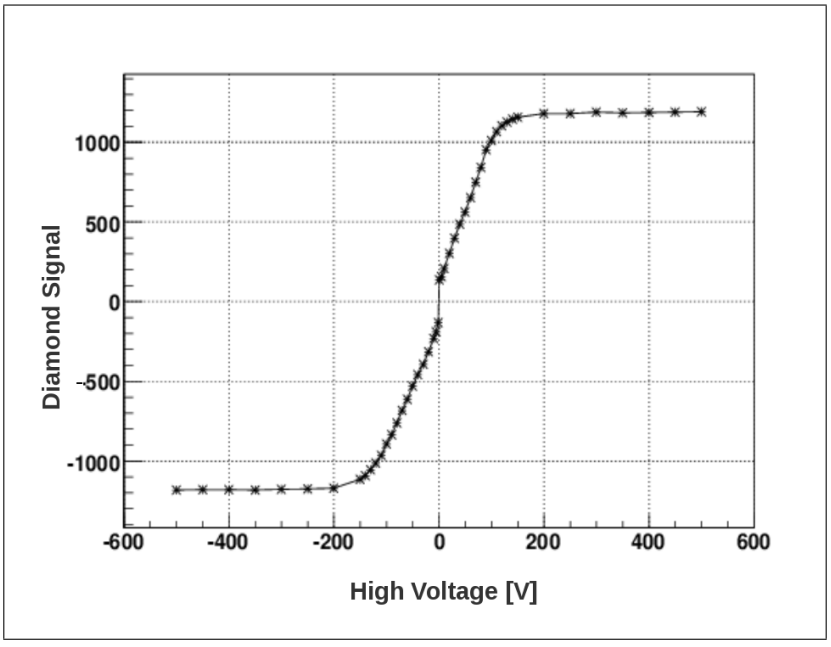

Figure 22: Measurement of the size of the diamond signals as a function of applied voltages.

It is visible that the signal is proportional to the applied voltage for lower voltages. Above a certain voltage (∼100 V for the measured diamond) the signal size remains constant. For voltages below

100 V the electrical field is too weak to separate all charge carriers and the electron-whole pairs can recombine. Above 100 V the electrical field is sufficient to separate all electron-hole pairs and the signal size remains constant. The information about the saturation voltage is needed to operate diamond sensors as particle detectors. Firstly, the signal-to-noise[7] ratio approaches a maximum. Secondly, the number of charged particle crossing the diamond is proportional to the signal (above 100 V).

7.2 Diamond Detectors at the LHC Based on pCVD

Diamond are used to measure particle rates inside the experiments of the LHC and also along the LHC ring with higher time resolution than ionization chambers. They measure beam losses at certain points along the LHC ring where large beam losses are expected, e.g. the injection region, beam dump region and beam cleaning region (see Sec. 6).
The first type of detector system is based on a pCVD diamond and the readout is done by oscilloscopes that give information about the amount of beam losses as a function of arrival time. These pCVD diamond detectors are installed in IR2 and IR8 (injection regions), IR3 and IR7 (cleaning regions) and IR6 (beam dump region). All pCVD diamond detectors are given in Table 2 with the corresponding trigger signal that starts the oscilloscope measurement.

Diamond detector location	Number of diamonds	Trigger signal	Purpose
IR2	1	injection trigger	beam loss measurements during injection
IR3	2	PM trigger	beam loss measurement in cleaning region
IR6	2	PM trigger	beam loss measurement in dump region
IR7	2	internal trigger	beam loss measurement in cleaning region
IR8	1	injection trigger	beam loss measurement during injection

Table 2: Location and trigger signal for the pCVD diamond detectors installed at the LHC.

In the dump and cleaning regions two diamond detectors are installed, one for each beam. The signal from each diamond detector is splitted in two channels with low and high amplifier gain to increase the dynamic range of the signal. The trigger signals for these diamond detectors are the post mortem (PM) trigger signal that is sent if the beam is dumped. It is also possible to use an internal trigger that can be adjusted in the oscilloscope. The internal trigger can be set to a certain signal amplitude and to a special beam loss pattern. Only if the oscilloscope observes beam losses above the threshold and the beam loss pattern fulfills a certain condition, the data is saved in an external buffer. A picture of the pCVD diamond detectors in the beam cleaning region in IR7 is given in Fig. 23 and measurements from these detectors are presented in Sec. 8.1.

[7] The signal-to-noise ratio is a comparison of the signal level to the background noise level. A high signal-to-noise ratio corresponds to a high quality signal and the noise level is low compared to the signal level.

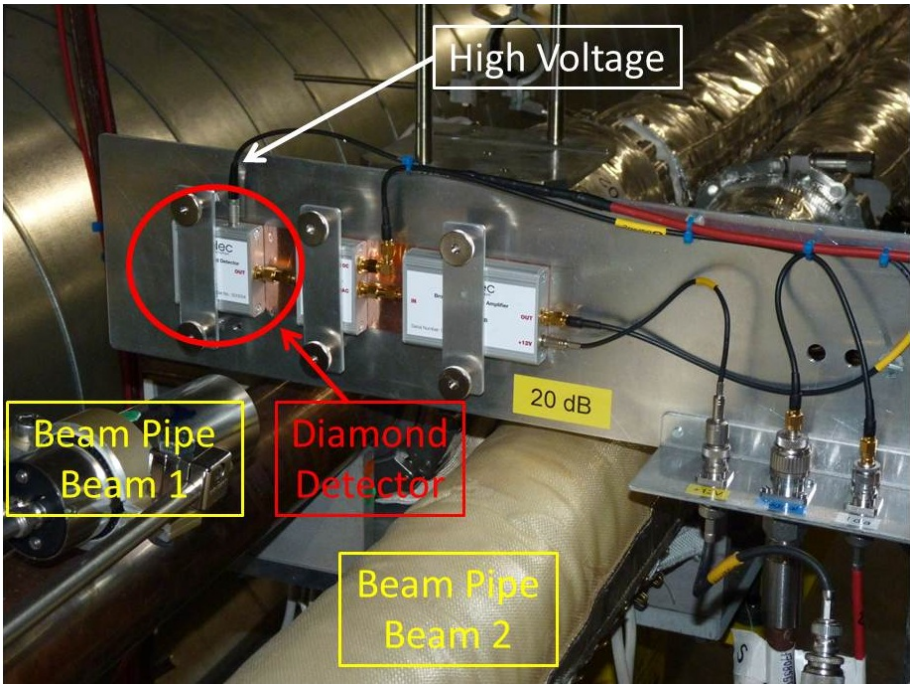

Figure 23: The pCVD diamond detector in IR7.

The diamond detectors in the injection regions are triggered by the injection trigger that is sent when a beam is transfered from the SPS to the LHC. Only one diamond detector at each injection point is installed downstream of the injection protection collimator (TDI). Each diamond signal is available with low and high gain.

7.3 Diamond Detectors at the LHC Based on sCVD

The second type of diamond detectors are made of sCVD diamonds and installed at locations with high beam losses (injection region, inside and outside of the CMS experiment) but also at locations with lower beam losses (RF regions). The readout electronics of all sCVD diamond detectors consists of a time-to-digital converter, an analog-to-digital converter and a scaler. The readout electronics is explained in Sec. 7.3.1.

These sCVD diamond detectors are used to monitor the beam halo (for example arrival time distribution) and also measurements of beam losses and the rates of collision products. Eight diamond detectors are installed inside CMS with a data processing in the CMS cavern. Six diamond detectors are installed around the LHC ring with data processing back-end part located at the CERN Prevessin side. A list of the locations and purpose of each sCVD diamonds is given in Table 3. These detectors take data continuously.

Diamond detector location	Number of diamonds	Purpose
IR2	1	counting losses at injection and arrival time measurements
IR4	2	counting losses and arrival time measurements
IR5 outside CMS	2	counting losses, beam halo, collision products and arrival time measurements outside of CMS
IR5 inside CMS	8	counting losses, beam halo, collision products and arrival time measurements inside of CMS
IR8	1	counting losses and arrival time measurement at injection

Table 3: Location and purpose of the sCVD diamond detectors installed in the LHC.

The eight diamond detectors in CMS are needed to measure the beam halo particles and collision products on each side of the interaction point in CMS. This system is explained in detail in Sec. 7.3.1 and measurements are presented in Sec. 8.2, 8.3 and 8.4.1. A picture of the four diamond detectors around the beam pipe on one side of the CMS interaction point is shown in Fig. 24.
The additional two diamond detectors installed outside CMS measure beam losses from bunches and collision products but with a lower rate. The need of the diamond detectors outside of CMS is to compare diamond measurements with measurements of ionization chambers installed at positions outside of the experiment. In that case, the amount of collision products that is able to penetrate the whole CMS detector at small angle can be observed with high time resolution.

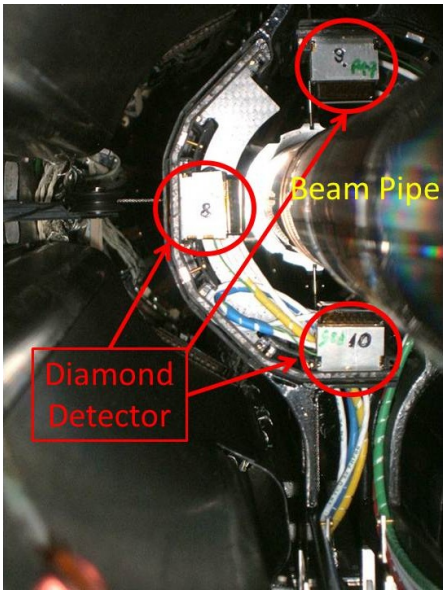

Figure 24: sCVD diamond detectors inside CMS (four detectors around the beam pipe on both sides of the interaction point).

The diamond detectors in IR2, IR4 and IR8 are used for both arrival time monitoring and beam loss rate measurements. The readout electronics can collect arrival time distributions mapped on a turn and collected over several minutes. In this distribution the bunch structure becomes visible,

allowing to monitor the beam loss intensity for each bunch. A picture of the installation in the LHC at IR8 is given in Fig. 25.

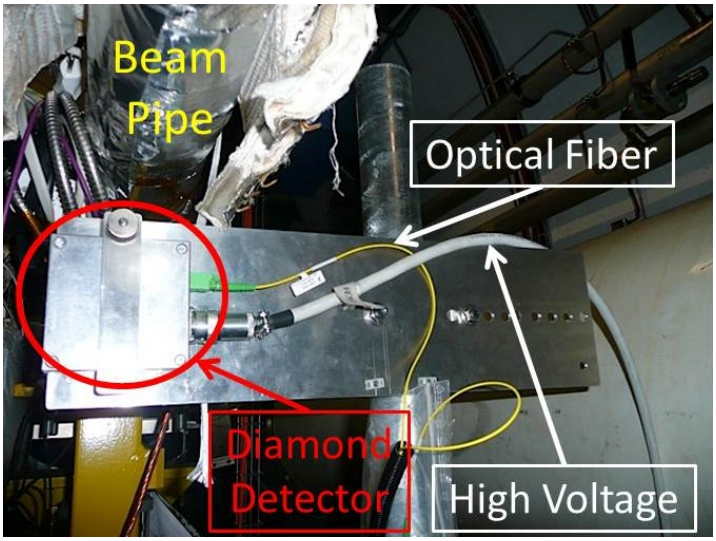

Figure 25: sCVD dioamond detector in IR8 below the beam pipe.

7.3.1 BCM1F and BRM System

The sCVD diamond detectors that are installed inside CMS are providing beam conditions to CMS and LHC. These detectors are explained now in detail.
The eight diamond inside CMS are also called **F**ast **B**eam **C**ondition **M**onitor (BCM1F). Four diamonds are located around the beam pipe on both sides of the interaction point of CMS as illustrated in Fig. 26.

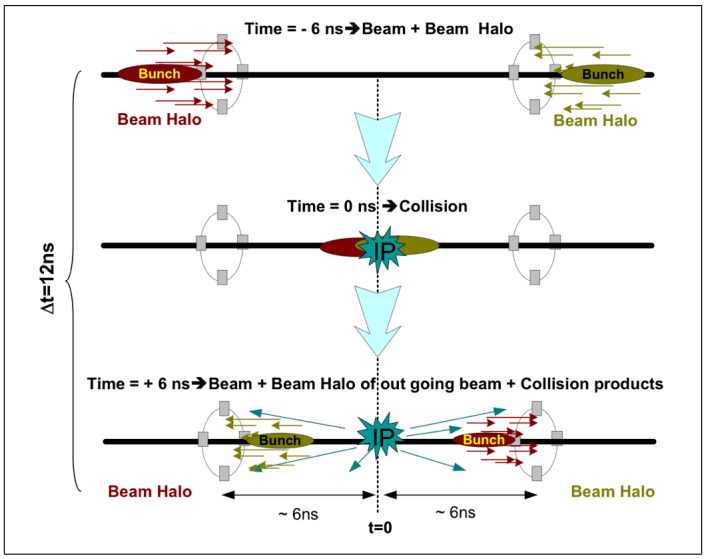

Figure 26: Layout of the BCM1F diamonds around the beam pipe inside CMS. The BCM1F detectors measure firstly beam losses of the incoming bunches on each side of the CMS IP. About6 ns later the bunches collide in the interaction point. Again 6 ns later the collision products and beam losses of the outgoing bunches are detected by BCM1F.

Each diamond has a volume of $5 \times 5 \times 0.5\,\mathrm{mm}^3$ and is metalized on both sides with a thin tungsten layer on top of a titanium layer. The distance between diamond and beam axis is 4.5 cm. They are 1.8 m away from the interaction point of CMS which is optimized to separate ingoing and outgoing particles. Particles with a speed of light need 6 ns for a distance of 1.8 m and the BCM1F system has a time resolution of 1.3 ns which is sufficient to measure bunch-by-bunch beam losses [23]. The losses originate from different mechanisms:

- beam halo: Protons with large betatron amplitude hit the collimators right before CMS and produce secondary particles. The secondary particles cross the beam pipe and are detected in the diamond sensors.
- beam gas collision: Protons interact with residual gas particles and produce collision products with sufficiently large scattering angle that they hit the diamonds.
- collision products: Two proton bunches collide in the interaction point of CMS and produce secondary particles that are detected by the diamond sensors.

Beam halo and beam gas are background rates inside the CMS and characterize the beam conditions. The collision rate is used to perform an online luminosity measurement of CMS. The arrival time measurements of these beam losses deliver a luminosity for each bunch crossing.
BCM1F is a part of the Beam Conditions and Radiation Monitoring System, BRM, that protects CMS in case of adverse beam condition and provides feedback to the LHC as for example the beam halo and beam gas flux or collision rates. The BRM system has several sub-detectors with different time resolutions and distances to the interaction point of CMS. Figure 27 shows a quarter of CMS with the main components of BRM relative to the interaction point of CMS. Table 4 lists all components with their time resolutions.

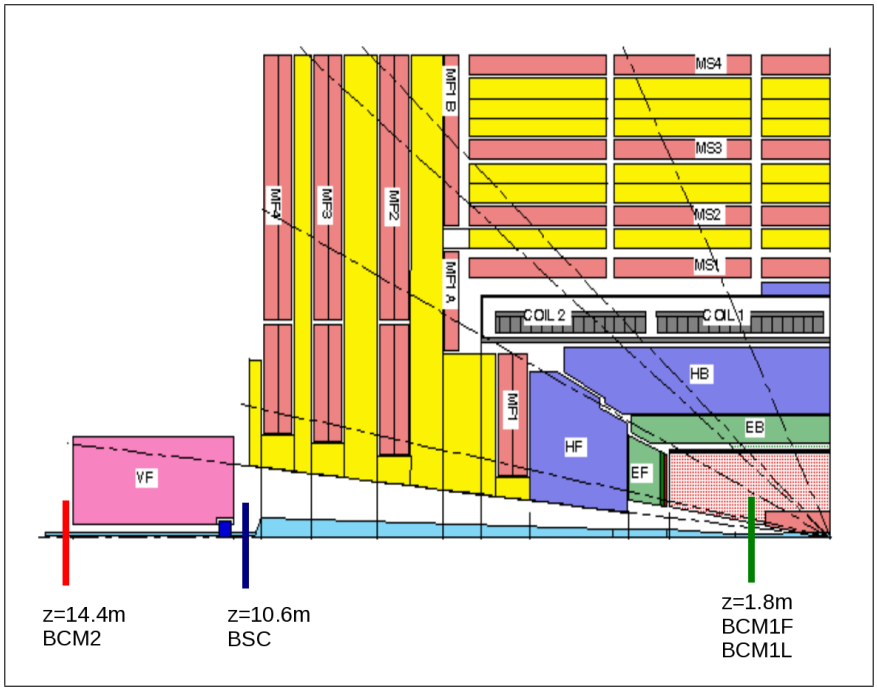

Figure 27: The position of the sub-systems (BCM2, BSC/BHC, BCM1L and BCM1F) of BRM inside CMS

sub-system	distance to interaction point	time resolution
BCM1F	1.8 m	ns (bunch-by-bunch)
BCM1L	1.8 m	40 μs
BHC	10.8 m	ns (bunch-by-bunch)
(old BSC)		
BCM2	14.4 m	40 μs
BPTX	175 m	200 ps

Table 4: Sub-systems of BRM

Additional Beam Condition Monitors (BCM1L and BCM2) based on pCVD diamonds are installed in CMS for protection. BCM1L is 1.8 m and BCM2 is 14.4 m away from the interaction point. Both sub-systems trigger a beam dump in case of a particle flux that is above the threshold as the ionization chambers. The readout electronic is the same as for ionizations chambers and therefore the time resolution is 40 μs. 12 different integration windows (from 40 μs till 83 s) are available to compare the measurements with the data of ionization chambers [24].
Beam Halo Counters (BHC) are also part of the BRM system. The BHC is an update of the older Beam Scintillator Counters (BSC). They provide a measurement of beam halo and collision products during low luminosity and high luminosity operation [25]. The distance to the interaction point is 10.8 m.
The last sub-system is the Beam Pick-Up Trigger Experiment, BPTX, that consits of four electrostatic botton electrodes which provide an electrical signal when a bunch passes by. It is therefore possible to measure the arrival time of each bunch providing a bunch timing for the CMS detector. It has a time resolution of 200 ps and a distance to the interaction point of 175 m [26].

7.3.2 Front-End and Back-End Electronics

The readout electronics of all sCVD diamond sensors is the same and consists of two parts, the front-end and back-end electronics.
Parts of the front-end electronics are the diamond sensor, the amplifier and the optical driver. The diamond sensor, amplifier and optical driver form the diamond detector. The back-end parts are the optical receiver and analysis modules (analog-to-digital converter, discriminator, time-to-digital converter, look-up-table and scaler). An illustration of the readout chain is given in Fig. 28.

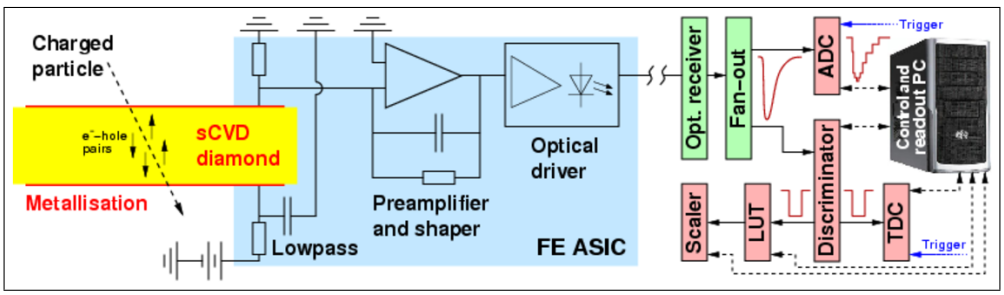

Figure 28: BCM1F readout chain. Left side: the front-end electronics with sensor, amplifier and optical driver. Right side: the back-end electronics with optical receiver and readout modules.

The diamond sensor, metallized on both sides, is glued to a contact on the amplifier printed circuit

board (PCB). A metallized sCVD diamond is shown in Fig. 29.

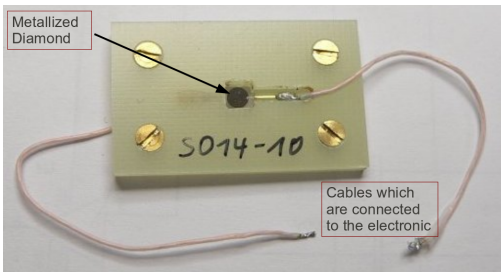

Figure 29: Diamond sensor with metallization in a plastic frame.

The sensor is integrated in the front-end amplifier as shown in Figure 28. When a charged particle crosses the diamond it produces electron-hole pairs which are separated due to the applied electrical field. The charge carrier drift produces a signal which can be amplified. The BCM1F amplifier is charge sensitive. It modulates an analogue optical signal via the optical driver.
The optical signal is transmitted to the counting room and an optical receiver converts it back to an electrical signal. The electrical signal is then distributed to several readout modules which have multiple input channels. The signals of the eight CMS diamonds for example are processed independently in each back-end electronic module. Therefore, every diamond sensors has its own channel number.
First, each electrical signal from each diamond sensor is fed into the corresponding input channel of a fan-in-fan-out unit that produces two copiesof each diamond signal. One signal is fed into an analog-to-digital converter and another signal from the same diamond is connected to a discriminator. The output signal from the discriminator is fed into:

- scaler: It is a unit for counting the incoming rates per second from each diamond sensor.
- time-to-digital converter: It measures the arrival time of each signal.
- look-up table: It receives input signals from different diamond sensors and provides logic combinations of the the signals.

A more detail description of all processing modules are given in the following paragraphs.

Analog-to-Digital Converter

An analog-to-digital converter, also called ADC, samples the signals produced by the diamond detector.
The flash ADC houses 8 channels and each channel samples 500 M samples/s corresponding to 2 ns time sampling. The memory buffer is 2 M samples long which corresponds to a memory buffer length of 4 ms. The buffer size for the sampling is adjustable and set to 90 μs. The ADC is triggered by the turn clock[8] every 89 μs that ensures the ADC sampling over one LHC turn.
A flash ADC contains a series of comparators. If the signal goes to the ADC it is compared with a unique reference voltage given by the comparators [27]. The produced output signal is then a binary output and therefore given in ADC counts or ADC bins.

[8]The turn clock is the revolution frequency of 11.25 kHz defined by the RF system.

Figure 30 shows an example of a sampled ADC signal from a particle that crossed the diamond at an arrival time of 70200 ns referred to the turn clock. The signal has a width of 100 ns and an amplitude of around 6 ADCcounts. The ADC baseline is at $\sim$ 80 ADCcounts. The width of the signal is determined by the amplifier shaping time.

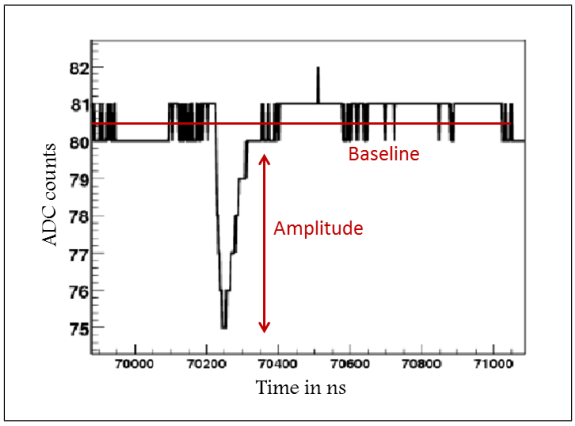

Figure 30: ADC signal from a particle that was measured with one of the sCVD diamonds around the LHC ring. The baseline is at 80 ADC counts and the arrival time of the signal, respect to the turn clock, is at 70250 ns. The signal has an amplitude of 6 ADC counts

The ADC measurement can be used for the analysis of amplitude spectra, arrival time distributions and monitoring baseline shifts due to e.g. a change of temperature of the laser driver.

Discriminator

Signals from a sensor pass through a discriminator that generates for each input signal above a certain threshold a standard output pulse. The discriminator that is used for BCM1F has 16 channels and each channel has its own threshold. It is set such that the electronic noise is suppressed. Only signals produced by charged particles generate an output signal. The discriminator output is a digital signal with rectangular pulse shape and with an adjustable width between 6 ns to 95 ns. Since the time between two consecutive bunches is at least 25 ns the output signal width is set to 14 ns. The signals from the discriminator go the analysis modules (look-up-table, time-to-digital converter, scaler).

Look-Up-Table :
The look-up-table (LUT) is a module with a field-programmable gate array (FPGA) that can be programmed by the user. The FPGA is able to produce coincidences of two or more input signals from different diamond detectors and it has a timer function. Coincidences of scaler rates are needed for the estimation of luminosity in CMS using BCM1F. Additionally, the LUT has an I/O register that is used to provide veto signals. Such veto signal is needed to block incoming signals and prevent a memory buffer overflow of modules like the time-to-digital converter.

Time-to-Digital Converter

The time-to-digital converter (TDC) measures the arrival time of signals. The used module houses

four TDC chips with 32 channels per chip. Only eight of the 128 channels are required for the BCM1F diamond sensors. The TDC contains an electronic clock that measures the arrival time of signals relative to a trigger, being the turn clock. This way an arrival time distribution over a whole LHC turn is produced. The minimum time between two input signals (double hit resolution) is 10 ns and the time resolution of the internal clock is 800 ps.
The arrival time information of the trigger and diamond signals are written in the TDC buffer that contains 32000 words. Each word contains information aboout:

- input channel number
- the arrival time of an incoming signal or the turn clock
- an identifier for a signal or the turn clock

The TDC buffer is read out after it is half filled (16000 words) with arrival time information. The readout is done with a block transfer and the information is successively filled into a second buffer, the ring buffer. The ring buffer is a memory area with 32000 words in a controlling computer. If the ring buffer is full, the incoming data overwrites the old data starting from the beginning of the buffer. All the time information about signal and turn clock is written in the ring buffer. An analysis program can then pick up a block of time information from the ring buffer and can analyse the arrival time of charged particle relative to the turn clock. Additionally, a post mortem analysis is possible. In the case of a beam dump the ring buffer contains still the information of the BCM1F signals from the last 100 ms before the dump.

Scaler

A scaler counts signals coming e.g. from the discriminator. The double hit resolution is 5 ns. The scaler has 16 channels and can therefore count signals from the eight diamond detectors and additional coincidence signals from the LUT. The BCM1F scaler provides the number signal within 1 s from the eight diamond detectors inside CMS and the coincidences from the LUT for the online luminosity estimation.
The data of the scaler is sent to the LHC control room as an estimation of luminosity, beam halo and gas rates. It is a valuable information to ensure low halo and gas rates inside the experiment.

7.4 Luminosity Measurements with BCM1F

The luminosity is an important parameter because it is neeeded to determine the cross section of all relevant physics processes. Additionally, a monitoring of the luminosity allows an optimization of the LHC operation towards maximal luminosity.
The BCM1F diamonds in CMS and their readout electronic can be used as a luminosity monitor since they detect collision products at low polar angle. Such an additional luminosity monitor would allow a real time luminosity monitoring even though the main data acquisition (DAQ) system is not working or the CMS detector does not take data.
The luminosity depends on several parameters as number of colliding bunches n_b, the revolution frequency f, the average number of inelastic collisions per bunch crossing μ and the inelastic

cross-section σ_{inel} [28]:

$$L = \frac{n_b f \mu}{\sigma_{inel}} . \tag{7.2}$$

The parameter that can be measured using BCM1F is the number of inelastic collisions μ. However, it has to be taken into account that all detectors have their own efficiency ϵ which depends on the luminosity and also on the number of bunches. Therefore, both parameters become:

$$\mu_{obs} = \epsilon_1 \mu \tag{7.3}$$

$$\sigma_{obs} = \epsilon_2 \sigma_{inel} . \tag{7.4}$$

The luminosity becomes therefore:

$$L = \frac{n_b f \mu_{obs}}{\sigma_{obs}} . \tag{7.5}$$

The observable quantity measured by the scalers is then:

$$\mu_{obs} = \frac{< N >}{n_b} , \tag{7.6}$$

where $< N >$ is the average number of particles crossing the diamond sensors within one LHC turn and n_b is the number of bunches in the LHC ring. Another luminosity estimation using accelerator parameters is given by:

$$L = \frac{N_1 N_2 f}{A_{eff}} , \tag{7.7}$$

where N_1 and N_2 are the number of particles in one bunch of beam 1 and beam 2 and f again the revolution frequency of the LHC [29]. The effective transverse area in which the collision takes place is A_{eff} and can be written as

$$A_{eff} = 2\pi\sigma_x\sigma_z , \tag{7.8}$$

where σ_x is the horizontal and σ_z the vertical beam width, assuming a Gaussian particle density distribution (definition of axes is given in Sec. 4). The beam width can be determined by so called van-der-Meer scans. In a van-der-Meer scan the beams are systematically displaced in small steps in the x- and z-direction during the collision process. Depending on the displacement the count rate of collision products will change as explained in [30]. For a maximum separation of the beams the count rate will become zero and for a zero separation or "head-on" collision a maximum count rate will be observed. The count rate as a function of time measured by the scalers will be Gaussian-like, allowing the estimation of the beam width.
The combination of Equ. (7.5) and (7.7) allows now the estimation of the cross section with the use of the van-der-Meer scan:

$$\sigma_{obs} = \mu_{obs}^{MAX} \frac{2\pi\sigma_x\sigma_z}{N_1 N_2} , \tag{7.9}$$

where μ_{obs}^{MAX} is the maximum interaction rate per bunch crossing measured by the detector. The results of the van-der-Meer scans for BCM1F can be found in [28].
The parameter that is needed for the online luminosity estimation is μ_{obs} which is estimated by the scaler rates from the eight BCM1F channels by combining different logics of the diamond detectors. The sensor locations of BCM1F is illustrated in Fig. 31.

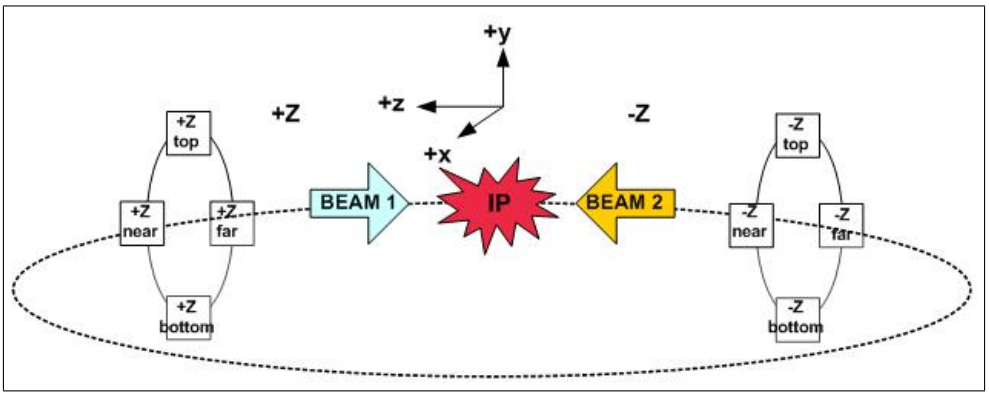

Figure 31: Layout of BCM1F diamond detectors. Four diamond detectors are located on the left side of the CMS interaction point (+Z) and four on the right side of the CMS interaction point (-Z).

The logic combination is done by the LUT that is described in Sec. 7.3.2 and produces the following logic combinations:

- XOR+: a logic OR of diamond signals from +Z
- XOR-: a logic OR of diamond signals from -Z
- OR: a logic OR of diamond signals from +Z and -Z
- AND: a logic AND of diamond signals from +Z and -Z .

The advantage of the different logic combination is a different sensitivity in different luminosity regimes. The rate of a certain logic combination defines the measured inelastic collisions μ_{obs} as described in [28] and [31] which are used to get a real time luminosity estimation.

8 Measurements at LHC and CMS

8.1 Beam Loss Measurements with pCVD Diamonds using an Oscilloscope

The MadX simulation showed that most beam losses are expected in the cleaning region IR7 where collimator jaws are very close to the beam center. The collimators are positioned 4-5 σ from the beam center which defines also the global aperture limit. All major beam losses that appear at any point in the LHC ring can be detected in IR7.
Therefore, it is reasonable to have diamond detectors near IR7 collimators to measure and analyse various beam losses. The pCVD diamonds that are installed in IR7 near beam 1 and beam 2 are able to detect various beam losses [32]. Beam losses due to injection, beam dump, beam instabilities and UFO events are analysed. The data is taken with an oscilloscope and an internal trigger is set to a certain beam loss threshold. If the beam losses are above the threshold the data is saved for offline analysis. The measurements with the diamonds were taken with a time resolution of 1 ns which allows a bunch-by-bunch beam loss analysis. In order to measure signals from single particles, the signal is amplified by 40 dB.

8.1.1 Beam Losses During Injection

The transfer of bunches from the SPS to the LHC is a complex process since the injection kicker pulse must be synchronized with the injected bunch. Additionally, the beam has to be injected as close as possible to the closed orbit. Otherwise the protons oscillate around the closed orbit and the many protons are lost. Such oscillations are called injection oscillation. Beam losses can be observed during each injection due to these injection oscillation [33].
A beam loss measurement with the pCVD diamond detector directly after the injection of 12 bunches is shown in Fig. 32.

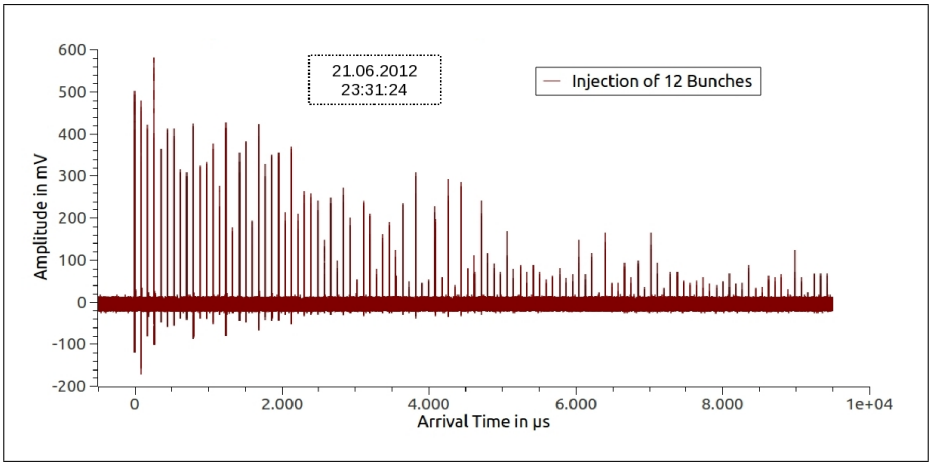

Figure 32: Beam losses during injection of 12 bunches as a function of arrival time. The time resolution is 1 ns and the diamond signal was amplified by 40 dB.

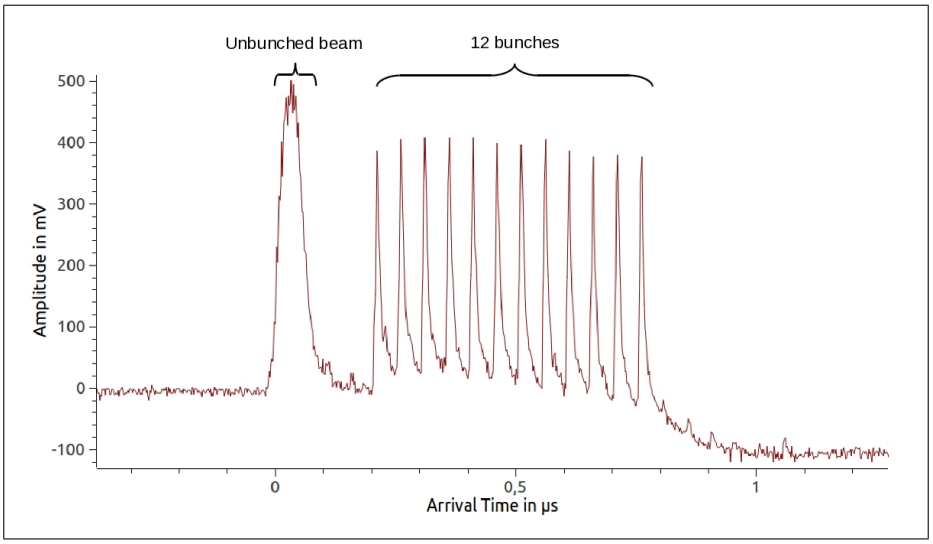

Figure 33: Zoom into the first beam loss spike. The 12 injected bunches are visible and separated by 50 ns. The beam loss before the 12 injected bunches is due to the unbunched beam.

The injection beam losses can be observed over 10 ms that corresponds to ∼110 turns. The spikes are separated by 89 μs due to the LHC revolution period. A closer look to the first beam loss spike is shown in Fig. 33. Two different types of beam losses can be observed. First, the losses from 12 injected bunches are visible with a separation of 50 ns. The beam loss amplitude is the same for each bunch. About 200 ns before is a Gaussian-shaped beam loss that cannot be caused by the injected bunches. It is believed that this peak is due to unbunched[9] beam from the previous injected circulating probe bunch that is lost during the rise time of the injection kicker magnet. A detailed explanation about beam losses due to unbunched beam is given in the next section (Sec. 8.1.2).

8.1.2 Beam Losses During Beam Dump

In case of a beam dump, the beam is extracted from the LHC rings by the beam dump kicker magnets (MKD) located in IR6 and sent via transfer lines to beam absorbers. The MKD deflects the beams from the circulating LHC trajectory to the beam dump transfer lines that connect the LHC ring with the beam absorbers. The beam absorbers intercept the beams in case of a beam dump.
Beam losses during the beam dump process are caused by losses during the rise time of the MKDs current. The waveform of the MKDs is illustrated in Fig. 34 showing the rising magnet current as a function of time between 101 μs and 104 μs. The 3 μs long rise time interval of the MKD current is synchronized with the abort gap (a particle free region) to ensure the deflection of the entire beam to the beam absorbers without large beam losses. Protons can nevertheless migrate into the abort gap [34]. These unbunched protons lead to beam losses during the rise time of the MKD current. Figure. 35 illustrates the process of beam losses during the MKD rise time. Due to the rise time, the protons are deflected by a certain angle.

[9]Protons that are not bunched but still circulating in the LHC ring. Such protons are e.g. in the abort gap.

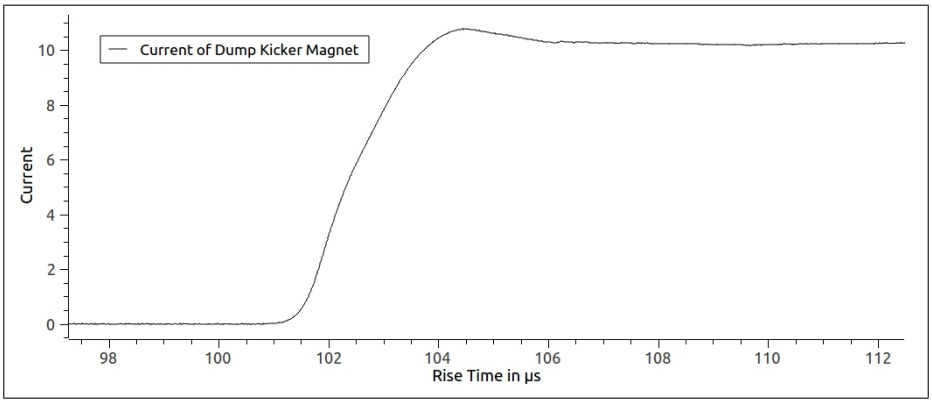

Figure 34: Current (in arb. unit) of the beam dump kicker (MKD) over time. The rise time from 101 μs to 104 μs is synchronized to the abort gap of 3 μs.

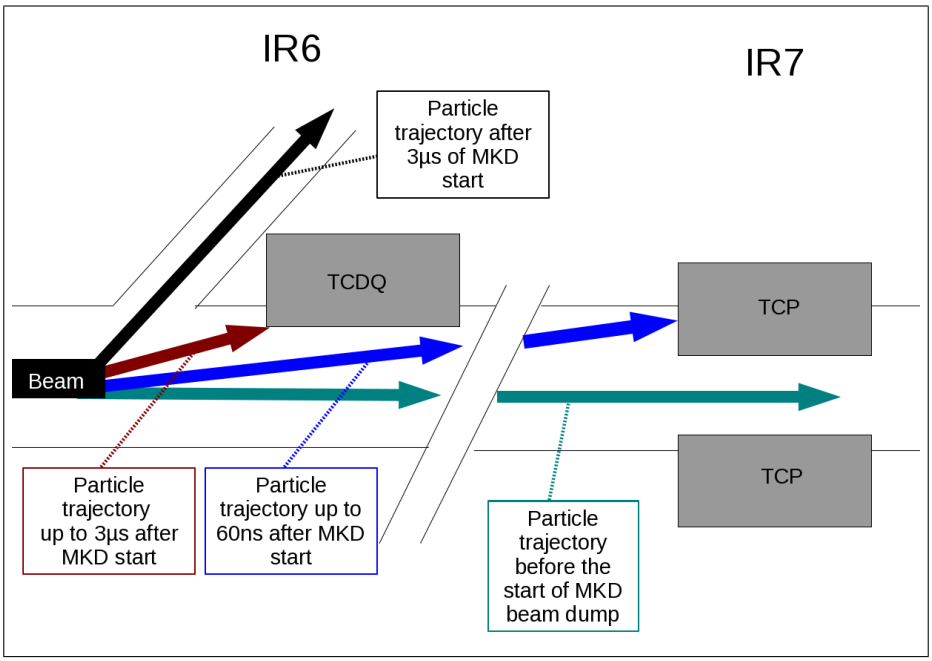

Figure 35: Particle trajectory during the rise time of the MKD. Protons in the abort gap are deflected to the collimators in IR6 and IR7.

At the beginning of the kicker pulse, protons in the abort gap are deflected with a small angle. They are not intercepted by the collimators in IR6 since the kick is too small but they are lost in IR7, the global aperture limit of the LHC ring. If the deflection angle is large enough, the protons from the abort gap are intercepted by the collimators in IR6. If the nominal current of the MKD is reached (at a rise time of 104 μs that is shown in Fig. 34), all protons are extracted to the beam dump transfer lines.
The lost protons in IR7 can be detected with the diamond detectors in IR7 and produce a typically Gaussian-shape beam loss as shown in Fig. 36.
The standard deviation of the Gaussian fit is typically 50-60 ns.

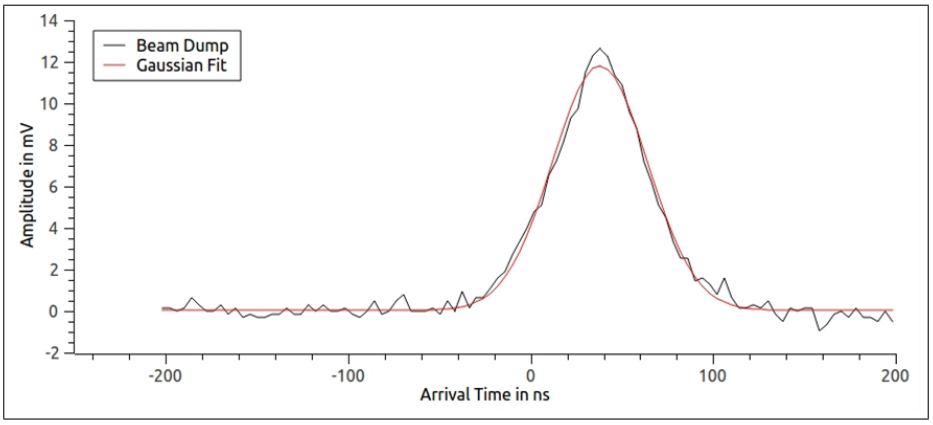

Figure 36: Beam losses as a function of arrival time during the beam dump from 08.05.2012 at 09:19:02. The diamond signal was amplified by 20 dB and the time resolution is 2 ns. The loss profile is typically Gaussian with a standard deviation of σ =50-60 ns.

8.1.3 Beam Losses Due to Instabilities

An instability of a beam produces beam losses during several seconds. Different mechanisms can lead to beam instabilities that are described in [35].
Beam instabilities often affect only a few bunches and it was frequently observed that an instability in one bunch can extend to neighbouring bunches or collision partner bunches. That can lead to significant beam losses which may exceed the dump thresholds and cause a beam dump. Figure 37 shows a measurement of the beam losses during an instability in one beam. The data covers $\sim$400 μs of beam loss measurements but the instability led to beam losses over 2 s.
The measurement shows that only a few unstable bunches contribute to the beam losses since only some beam loss spikes are visible. One of the spikes appears at the arrival time of 560 μs (0. Turn in Fig. 37) and a zoom of that spike is shown in Fig. 38(a). It shows six bunches with a spacing of 50 ns. After 266 μs that correpsonds to 3 turns (3. Turn in Fig. 37) a similar loss pattern with six bunches can be observed as illustrated in Fig. 38(b). This effect is caused by the LHC tune of $Q_x = 64.31$ (horizontal) and $Q_y = 59.32$ (vertical) with a fractional tune of ~ 0.31. Therefore, the loss amplitude is modulated with a periodicity of $\sim$3 turns. Figure 38(c) shows the same bunches after the first turn and Fig. 38(d) after the second turn. The loss amplitude is much smaller for the second and especially for the third turn due to the change of the phase advance.

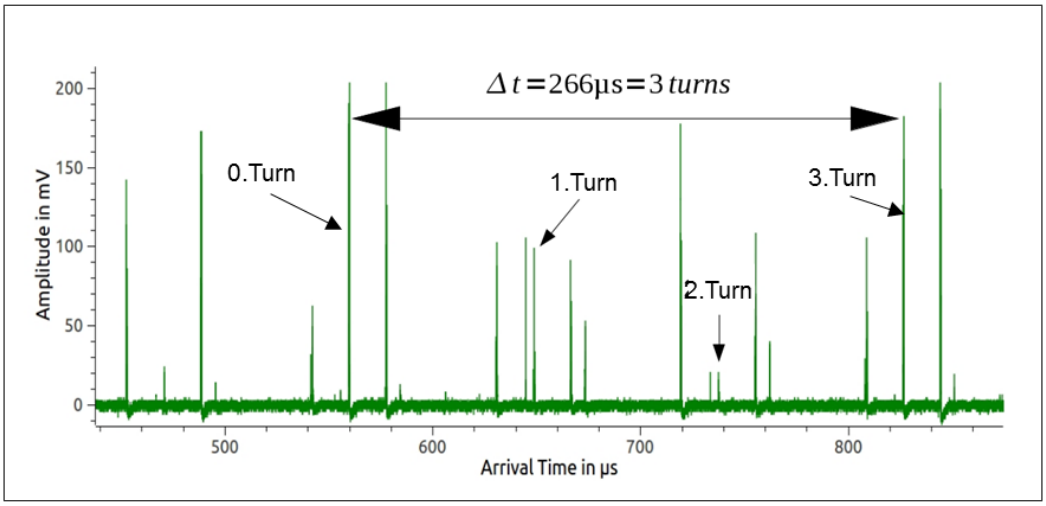

Figure 37: Measurement of instability in beam 1 from the 29.05.2012 at 15:42. The beam losses were detected during 2 s. A similar loss amplitude can be observed every 3 turns due to the fractional tune of ∼0.3. Signal amplification: 20 dB. Time resolution: 2 ns.

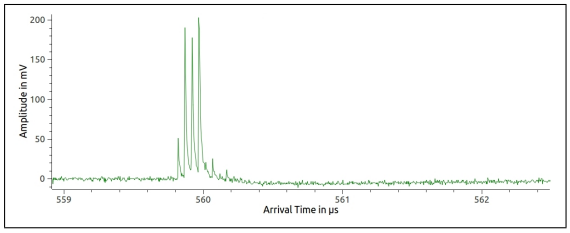

(a) Zoom of unstable bunches at an arrival time of 560 μs (0. turn in Fig. 37). Six bunches that are separated by 50 ns contribute to beam losses.

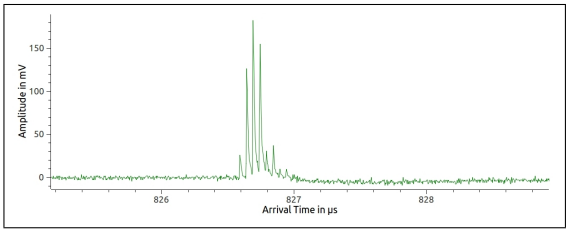

(b) Zoom of the same six bunches but three turns (∼266 μs) later (3. turn in Fig. 37). The beam loss pattern is still the same due to the fractional tune of ∼0.3 and the periodicity of 3 turns.

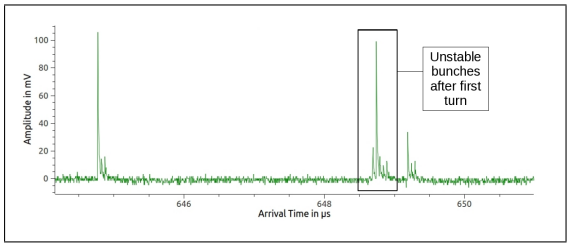

(c) Zoom of the unstable bunches after the 1. turn (see Fig. 37). The beam loss amplitude is less due to the change of the phase advance.

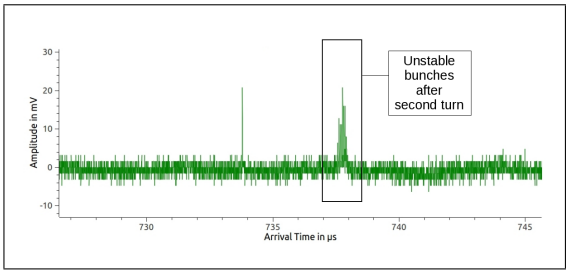

(d) Zoom of unstable bunches after the 2. turn (see Fig. 37). Only small losses compared to the first or third turn can be observed.

Figure 38: Closer look at unstable bunches at an arrival time of 560 μs and after one, two and three turns.

8.1.4 Beam Losses Due to UFO Events

UFO events lead to beam losses in each bunch as explained in Sec. 5. The elastic scattered protons can be detected in IR7 with the diamond detectors. Several UFO events with a time resolution of ∼1 ns were observed with the diamond detectors in IR7. One measurement is shown in Fig. 39. It shows two UFO events that occur in the injection region one after another. First, a very small

beam loss pattern is visible and after 100 μs a larger UFO event appears. The second UFO loss profile is Gaussian as already seen in previous measurements with ionization chambers.

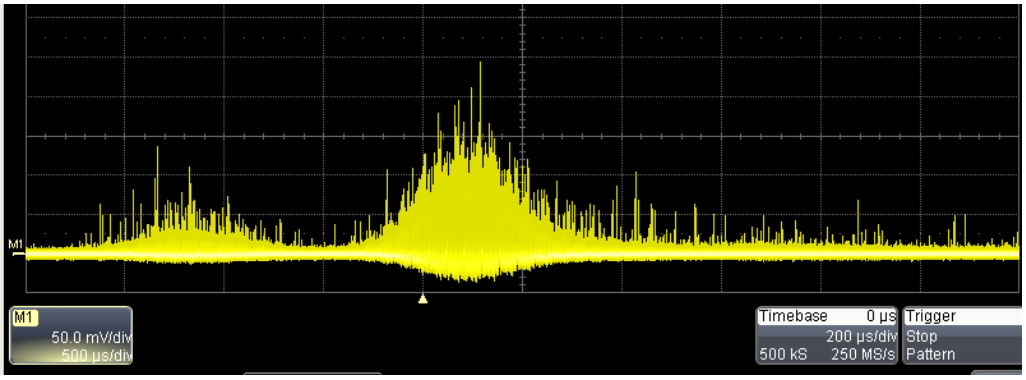

Figure 39: Measurement with oscilloscope of two UFO events one after another. The typical beam loss profile of an UFO event is Gaussian. The UFO event occurred in the injection kicker at IR2 in beam 1 on the 20.08.2012 at 18:07. Time axes: 200 μs/div.

Another large UFO event that dumped the beam when the beam losses were still increasing is shown in Fig. 40. After a rise time of ~600 μs the beam was dumped. The beam losses due to the beam dump are also visible (see Sec. 8.1.2). A zoom into the last part of the beam losses before the beam dump in Fig. 41 shows the filling pattern of the LHC (12, 144, 144, 72, 144, 144, 72, 144, 144, 72, 144, 144 bunches). It confirms the assumption that all bunches contribute to beam losses. Another zoom of the last 36 bunches before beam dump (Fig. 42) shows clearly 36 bunches that are separated by 50 ns. The last beam loss is due to unbunched beam in the abort gap when the beam is dumped (see Sec. 8.1.2).

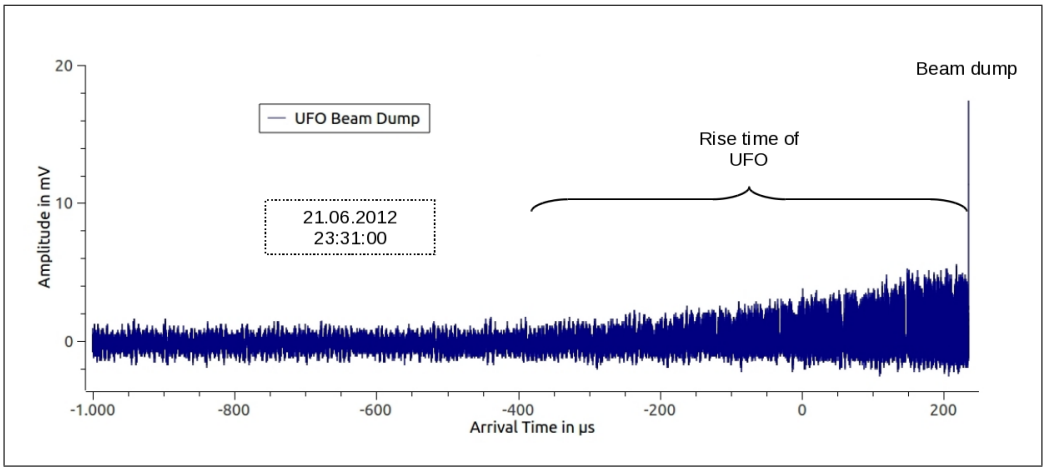

Figure 40: Beam losses over arrival time due to an UFO event. The beam was dump at the rising edge of the beam loss profile. The rise time of the UFO event is ~600 μs (7 turns). Signal amplification: 20 dB. Sampling time: 2 ns.

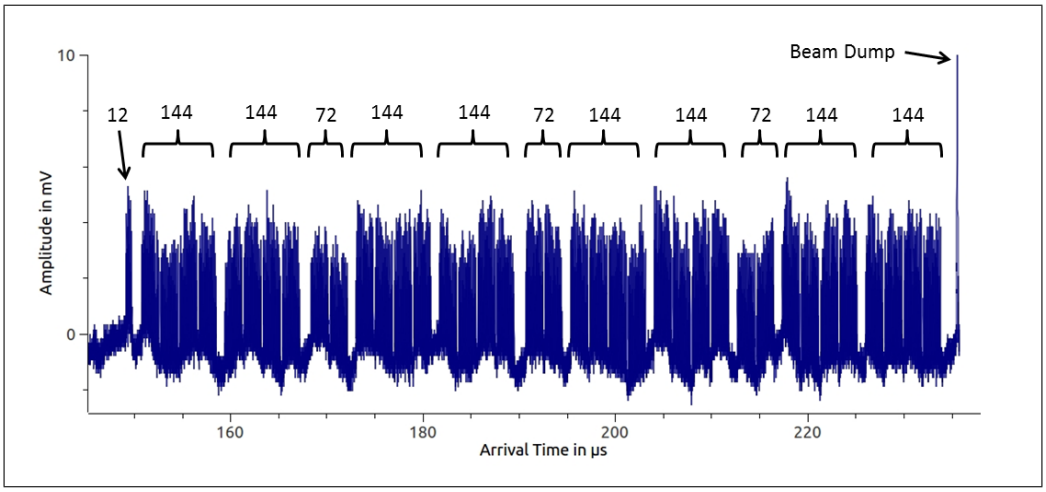

Figure 41: Zoom into the last beam losses before the beam dump. The injection scheme is visible (12, 144, 144, 72,... bunches).

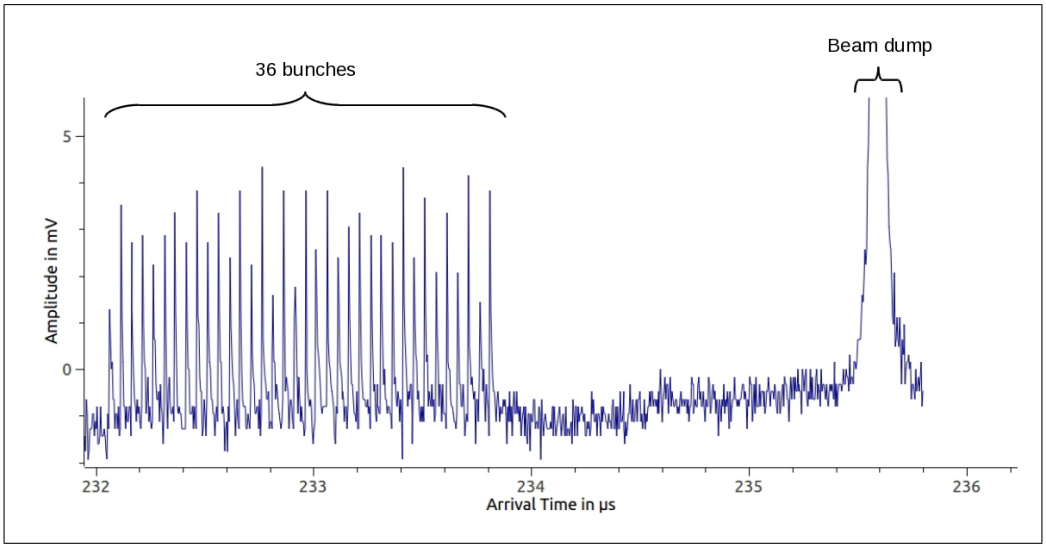

Figure 42: Zoom into the last bunches before the beam dump. 36 bunches with 50 ns spacing are visible and also the beam loss due to the beam dump.

8.2 ADC Measurements from sCVD Diamonds

The signals of the sCVD diamond detectors from the BCM1F systems are processed with the readout electronics as described in the previous Sec. 7.3.1. One of the readout modules is the ADC which provides a detailed information of the incoming signals due to beam losses or collision products. A signal sampling of 2 ns allows a detailed analysis of the signal amplitude, signal length and the arrival time. It is therefore possible to provide amplitude spectra or arrival time distributions, mapped on one LHC turn, collected over several minutes.

8.2.1 Amplitude Spectra

An amplitude spectrum contains information about the noise, MIP (minimum ionizing particle) amplitude and saturation of the front-end electronics. Depending on the location of the sCVD, the amplitude spectra looks different. Two typical amplitude spectra from different sCVD positions are shown in Fig. 43 and Fig. 44. Figure 43 shows an BCM1F amplitude spectrum measured with diamond detectors in CMS. A noise peak below 4 ADC counts is visible. The peak that corresponds to a MIP signal is at ∼7 ADC counts. The dip between the noise and MIP peak defines the thresholds for the discriminator. The peak at ∼75 ADC counts is due to the limit of the dynamic range of the optical driver in the front-end electronics and shows the saturation of the front-end electronics.
The amplitude spectra in Fig. 44 was taken with the diamond detector in IR8 and represents a typical amplitude spectra from sCVD diamond detectors in the LHC tunnel. A clear MIP peak cannot be observed due to the small amplitude of MIP signals. Only the noise peak at very small amplitudes is visible and also the saturation peak of the front-end electronics at 34 ADC counts. The reason is very likely a low signal-to-noise ratio in the front-end and laser driver.

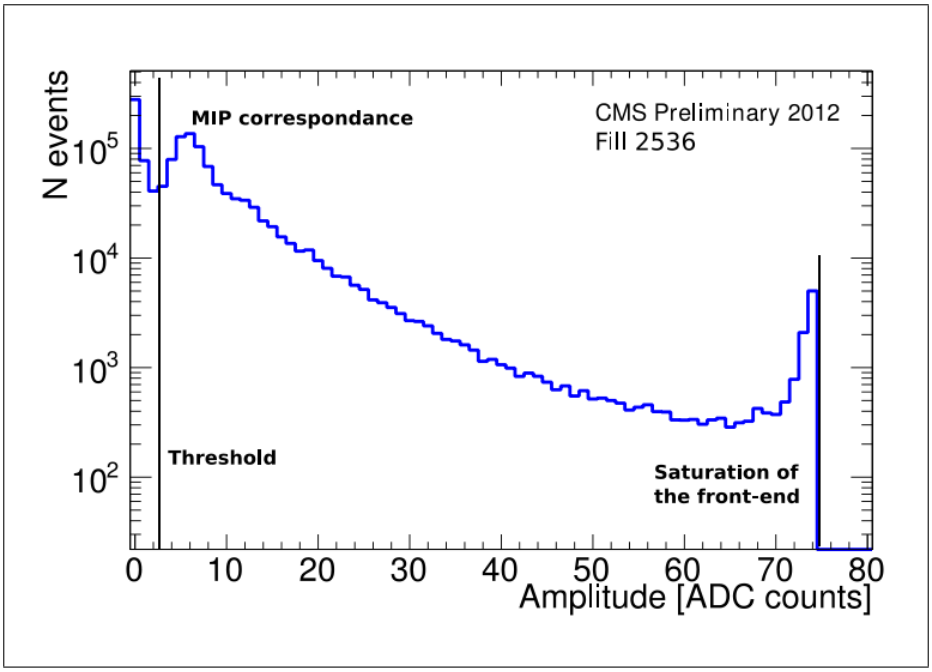

Figure 43: Amplitude spectrum from a BCM1F diamond detector in CMS measured with the ADC. Noise signals have small amplitudes. The signal amplitude of MIPs is at ∼7 ADC counts. The saturation peak at ∼75 ADC counts is due to the dynamic range of the front-end electronic of the diamond detector.

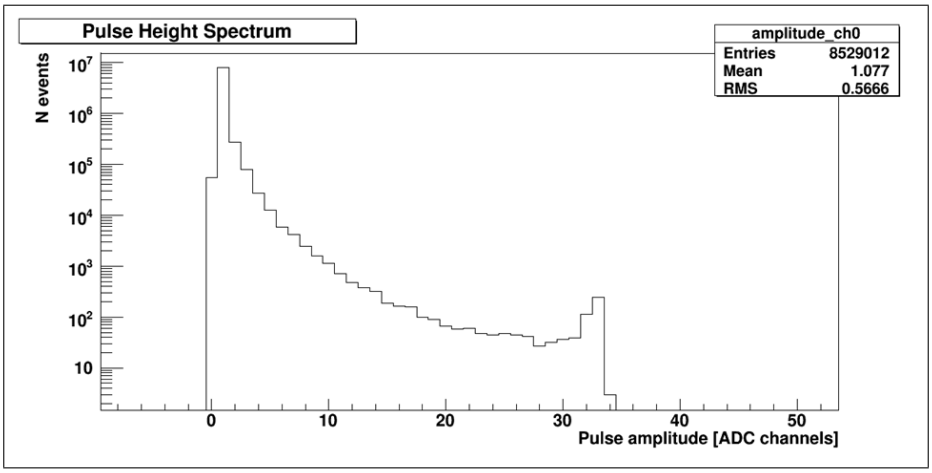

Figure 44: Amplitude spectra from sCVD diamond detector in IR8. A large number of signals with small amplitudes is visible. A clear MIP peak cannot be observed. The saturation of the front-end electronics is at 34 ADC CH.

8.2.2 Arrival Time Distribution

The ADC measurement of the arrival time of incoming signals with respect to the turn clock is collected over many LHC turns (∼30 min). Therefore, a signal distribution within a LHC turn is provided. Arrival time distributions depend on the location of the diamond detector, the LHC fill pattern and the collision pattern in the four main experiments. Of interest is the arrival time of the abort gap. A special characteristic of the abort gap can be observed in CMS and ATLAS where the abort gaps of beam 1 and beam 2 are synchronized in the interaction points. Both abort gaps have therefore the same arrival time. This is not the case for the interaction point in ALICE and LHCb.

A typical arrival time distribution from BCM1F in 2012 measured with the ADC is shown in Fig. 45.

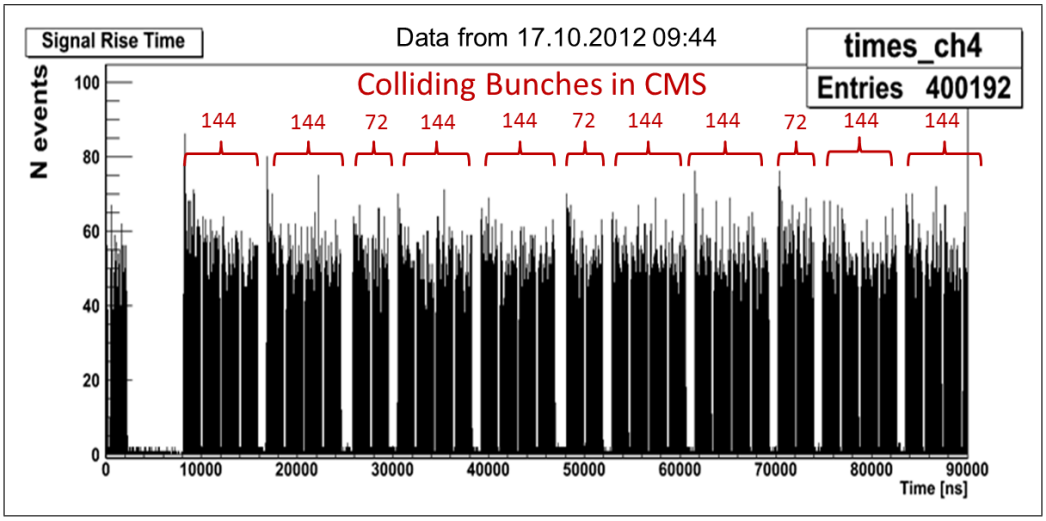

Figure 45: Arrival time distribution of signals from BCM1F measured with the ADC. The bunch structure of the CMS collision scheme is visible. A non-colliding sequence is visible containing the abort gap.

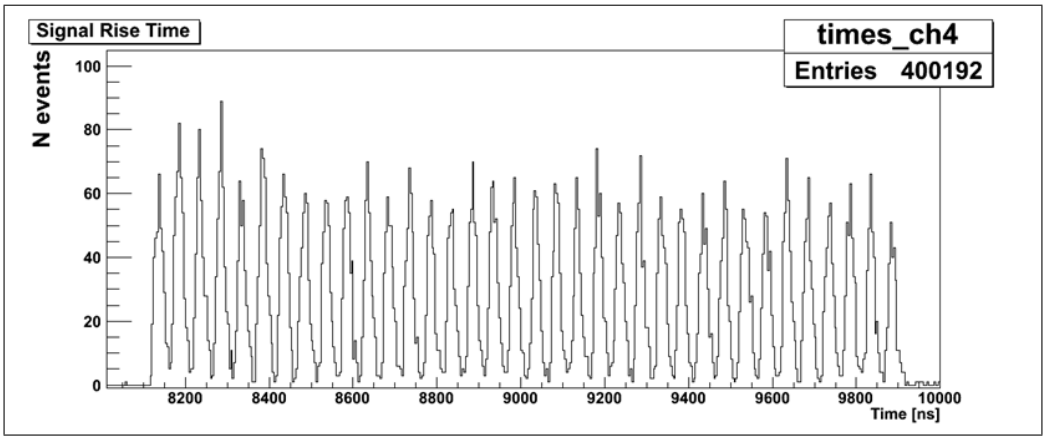

Figure 46: Zoom into the first bunches after the abort gap. A bunch spacing of 50 ns is visible.

The signals are dominated by the collision products from the CMS interaction point. Therefore, the time pattern of colliding bunches in CMS is visible. The gap without bunches is due to the particle free abort gap of 3 μs plus non-colliding bunches (6 non-colliding bunches in CMS[10]). A zoom in the first bunches after the gap is shown in Fig. 46. It shows one train with 36 bunches spaced by 50 ns. Another arrival time distribution is shown in Fig. 47 and is taken from the sCVD detectors in IR8. These signals are also dominated by collision products coming from the LHCb interaction point. Two beam free gaps are visible that are due to two non-colliding sequences.

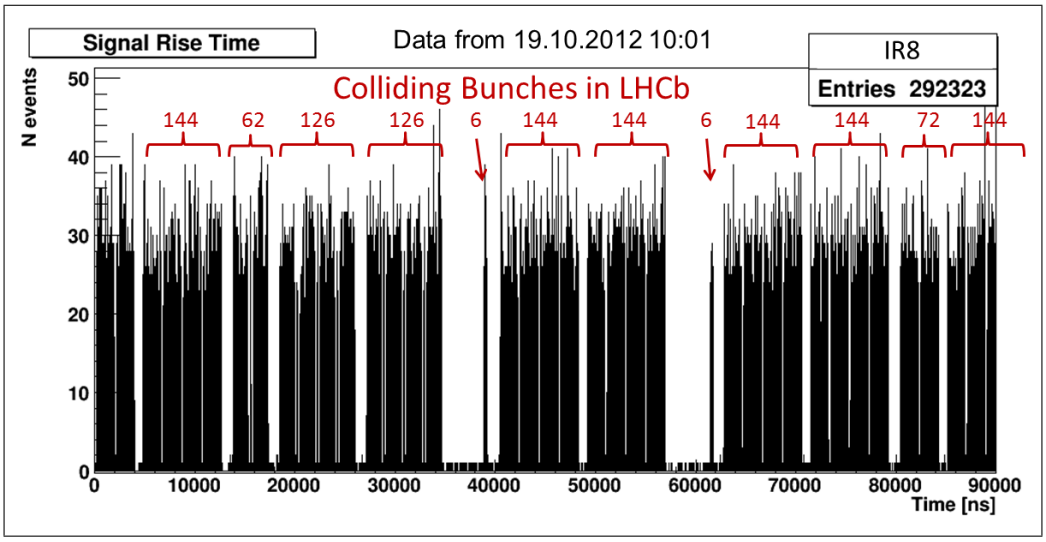

Figure 47: Arrival time distribution of signals from sCVD diamond detector in IR8. The signals are dominated by collision products. The plot shows two signal free gaps due to two non-colliding sequences.

8.3 Arrival Time Measurements with a TDC from sCVD Diamonds

To measure the arrival time distribution of signals, a TDC instead of an ADC is used because of several reasons. First the ADC produces a large amount of raw online data (file sizes in the order

[10]The injection scheme in the LHC was: 6, 144, 144, 72, 144, 144, 72, 144, 144, 72, 144, 144 bunches. The collision pattern in CMS was: 144, 144, 72, 144, 144, 72, 144, 144, 72, 144, 144

of GB) and in addition an offline analysis is needed that takes a lot of time. The TDC saves only the arrival time information and the offline analysis is much faster. The analysis program collects the time information of signals over many LHC turns and creates an arrival time histogram with the turn clock as a reference. To see a clear bunch pattern, the integration is set to about 10 min. The arrival time of signals with respect to the turn clock is converted to the corresponding bunch number that follows the LHC bunch numbering scheme, allowing an identification of each single bunch. It has to be pointed out that such a conversion is only possible for the CMS BCM1F signals since all colliding and non-colliding bunches are synchronized in CMS due to the synchronized abort gap of beam 1 and beam 2.

8.3.1 TDC Histograms from IR5

The TDC histogram shown in Fig. 48 was measured with the BCM1F detectors in CMS in 2010.

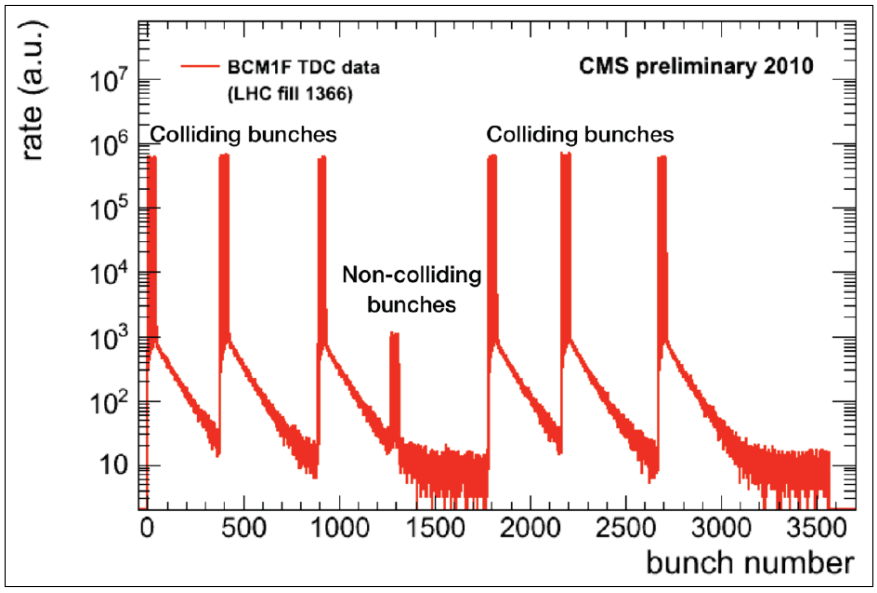

Figure 48: Signal rate from BCM1F diamonds in CMS over bunch number. Colliding and non-colliding bunches are clearly visible. The signal rate for colliding bunches is three orders of magnitude higher than for non-colliding bunches [taken from R. Walsh, DESY].

It shows the number of incoming signals as a function of bunch number within a LHC turn. The beam in this fill contains seven trains and each single train has eight bunches. The TDC histogram shows that it is possible to differentiate between colliding and non-colliding bunches in CMS because the signal rates of the colliding bunches are three orders of magnitude higher than the rates of non-colliding bunches. After each colliding bunch a long tail of exponential shape with a lifetime of $\sim$2.12 μs is observed [36]. This tail is called "Albedo Effect" and it is due to slow particles crossing the sensor after collision. These particles might be collision products that reach the endcaps of the electromagnetic calorimeters (ECal) of CMS[11] and then reflected to the BCM1F diamonds. Additionally, the collision products excite the material around the BCM1F diamonds which subsequently decay. A Monte Carlo simulation showed that the albedo tail is caused by

[11] The ECal endcaps are illustrated in Fig. 27 and marked with "EF". They have a larger distance to the interaction point of CMS than the BCM1F diamonds. Therefore, the reflected particles have a longer time of flight. The ECal is a detector for electrons and photons.

neutrons, photons, electrons and positrons with a later arrival time as presented in Ref. [37]. Another TDC histogram with collisions in CMS is shown in Fig. 49. The measurement was done with a sCVD diamond next to CMS, monitoring the rate of collision products outside of CMS. The signals are dominated by collision products and the colliding bunch pattern in CMS is visible. This TDC data is taken in 2012 with a larger number of bunches in the LHC. The long sequence with a low rate is due to the abort gap and non-colliding bunches. The non-colliding bunches are also visible but with a much lower rate (∼2 orders of magnitude).

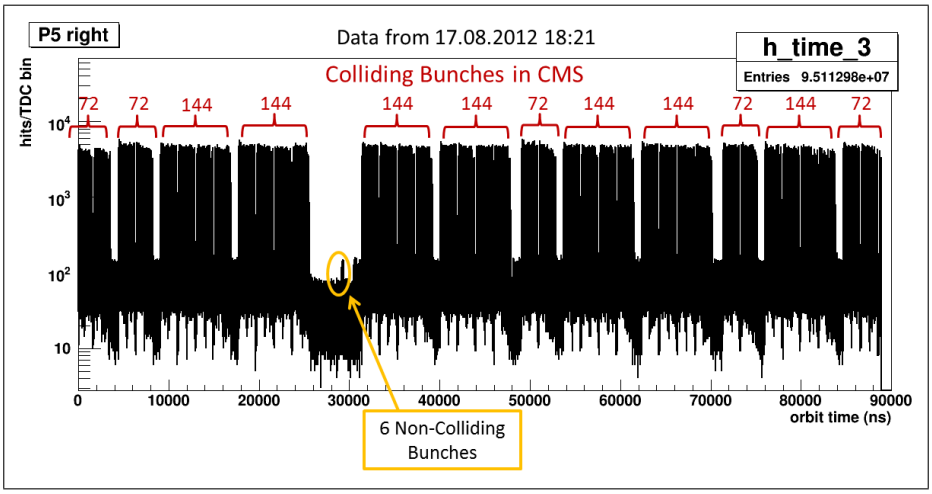

Figure 49: Signal rates from sCVD diamond detector next to CMS over arrival time respect to the LHC turn clock. The data was taken in August 2012. The signals are dominated by collision products in CMS. Therefore, the colliding bunch pattern from CMS is visible.

8.3.2 TDC Histograms from IR4

A TDC histogram from a detector at a location where the beams do not collide is shown in Fig. 50. The detector in IR4 is more sensitive to beam 2. The sensitivity to one of the beams is clearly visible in the histogram since the bunch structure for beam 2 can be observed (6, 144, 144, 72, 144,... bunches). The gap between the last bunch of the 144 bunch train and the six bunches is the particle free abort gap which is ∼4.5 μs long as defined by the LHC. The rate coming from beam 1 is lower. Some bunches (two times 36 bunches) of beam 1 can be observed in the abort gap of beam 2. The histogram also shows that the abort gap is not synchronized. Both beams are overlapping and the abort gap of beam 1 and beam 2 are not synchronized in IR4. In general, the rate at IR4 histogram is lower compared to the rate in IR5 since the diamonds in IR4 detect only beam losses due to residual gas particles and not due to collision products.

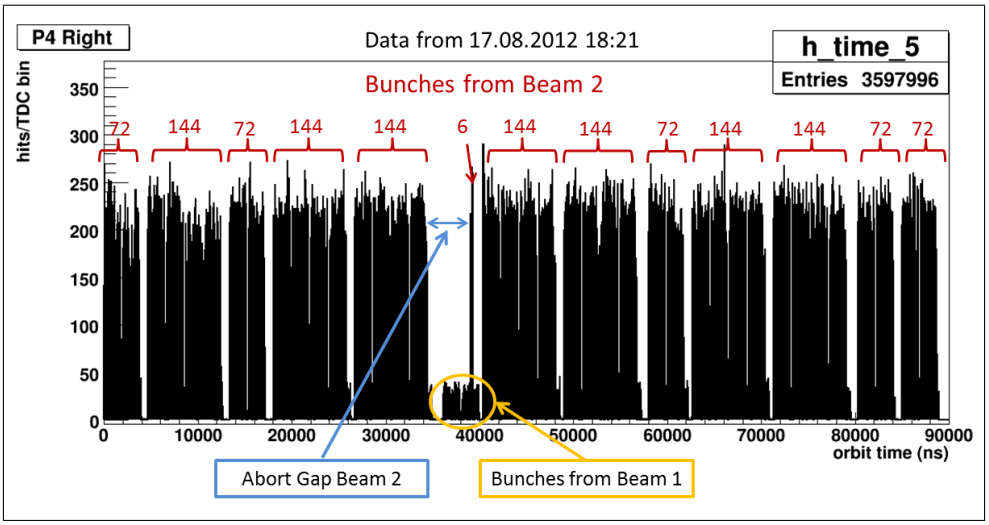

Figure 50: Signal rate over arrival time with respect to the turn clock measured in IR4 in August 2012. Signals coming from beam 2 have a higher rate than beam 1 signals since the sCVD diamond is located above the beam pipe of beam 2.

8.3.3 TDC Histograms from IR8

The histogram in Fig. 51 shows the signal rate in IR8 as a function of time respect to the turn clock. It is dominated by collision products as in the case of IR5. A comparison between the arrival time measured with ADC (Fig. 47) and the arrival time measured with TDC (Fig. 51) shows as expected the same bunch pattern.

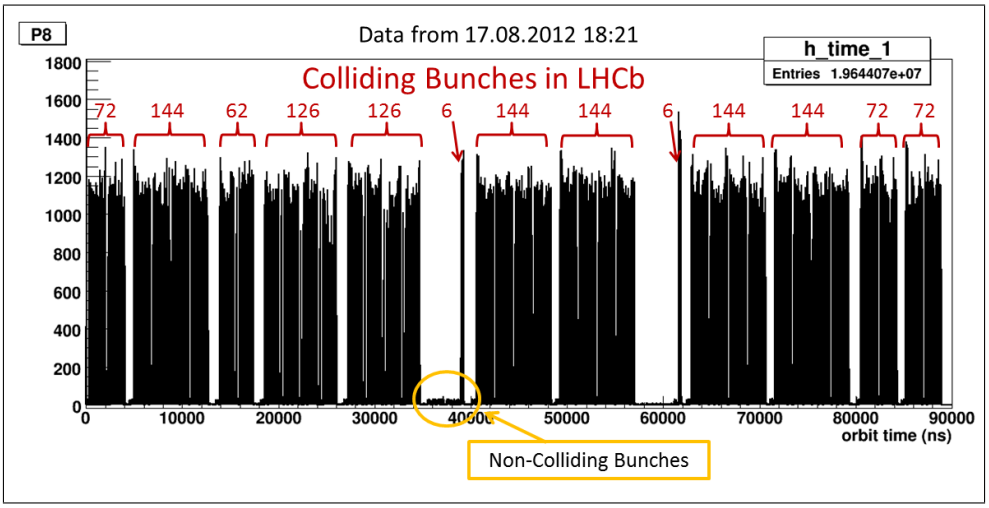

Figure 51: Signal rate as a function of time respect to the turn clock measured in IR8 in August 2012. The rate is dominated by collision products and the two sequences with low rate are due to non-colliding bunches and particle free gaps.

The TDC data shows two sequences without high rates, coming from collisions at the interaction point of LHCb. In the first non-colliding sequence also signals from non-colliding bunches of beam 2 with low rate can be observed. During the time of the second non-colliding sequence, beam 1 is arriving but the detector in IR8 is sensitive to beam 2. Therefore, the beam loss rate of beam 1

cannot be observed. This example shows that in the TDC signals from colliding bunches and also non-colliding bunches from beam 2 are visible in the same histogram. The non-colliding bunches from beam 2 are not visible in the ADC histogram shown in Fig. 47 due to the lower statistics for the ADC measurement.
Data which have been taken in 2011 (see Fig. 52) shows a part of an older TDC measurement of signal rate in IR8. Bunches with low and high rates are visible. The time between the first low rate and the first bunch with higher rate is 470 ns, corresponding to a distance of 141 m, assuming particles travel with the speed of light. That observation can be explained by the position of the detector with respect to the interaction point of LHCb which was ∼70.5 m (the distance was changed at the end of 2011 to 69.2 m for an optimized arrival time measurement). The first bunch from beam 2, that produces small beam losses, travels from the diamond to the interaction point of LHCb. The bunch needs 235 ns to travel a distance of 70.5 m. This bunch from beam 2 collides with another bunch from beam 1 and collision products are produced. The collision products plus the beam losses from beam 1 travel from the interaction point of LHCb to the diamond detector and they need again 235 ns for that distance. The larger spikes in the TDC histogram are therefore coming from collision products and beam 1. That explanation is also illustrated in Fig. 53.

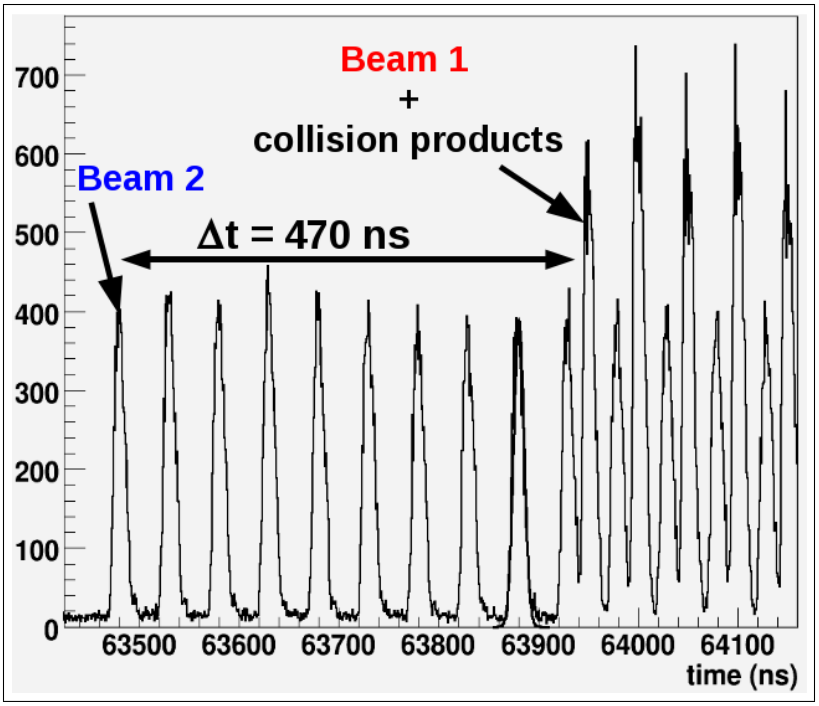

Figure 52: Particle rate as a function of time respect to the turn clock from IR8 during collision from 2011. The difference in the rate of colliding and non-colliding bunches is visible and also the time that is needed by a relativistic proton travel from the detector to the interaction point of LHCb.

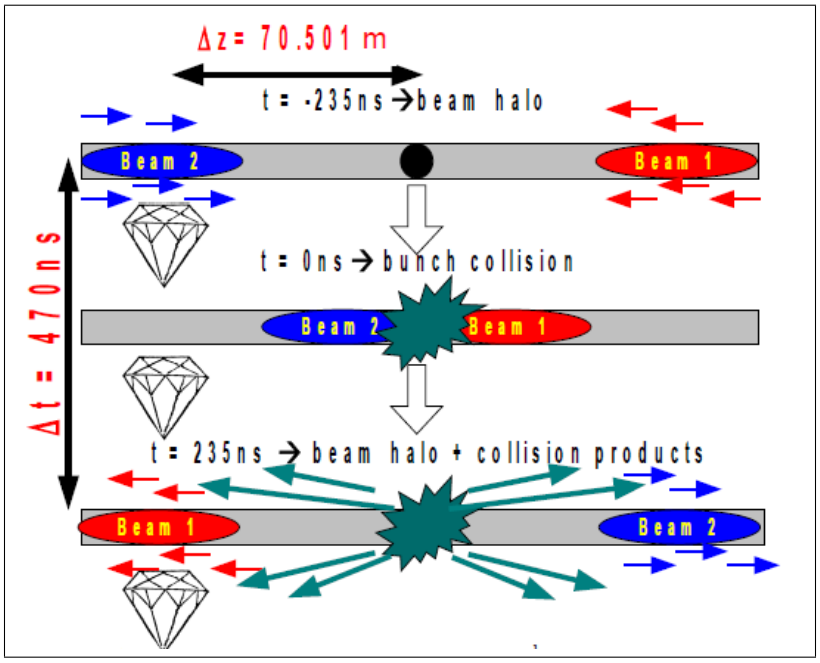

Figure 53: Illustration of a bunch that travels from the position of the diamond detector to the interaction point of LHCb.

8.4 Count Rates using Scalers from sCVD Diamonds

In order to measure the evolution of beam losses during a LHC fill diamond detectors are used. In addition, these detectors are useful to monitor the vacuum quality and beam collision. All beam losses are sent to the scalers and counted over 1 s, a time small enough to see variation of beam conditions but high enough to have sufficient statistics.

8.4.1 Scaler Rates in CMS

Figure 54 shows scaler rates from BCM1F in CMS when LHC is filled with heavy ion beams. Clearly visible are the rates at different stages of the LHC operation mode: injection, ramp, flat top, squeeze, adjust and stable beam.
The rates at the beginning (marked in grey) are due to noise and cosmic particles that hit the diamond sensor. As soon as the LHC injects the beam the beam losses increase (marked in green) due to injection oscillations (see Sec. 8.1.1). Beam losses also appear during the acceleration (marked in blue) because of two effects:

- Unbunched particles are lost during the acceleration because of the change of the momentum.
- The collimator settings are changed to a smaller half-opening and therefore more particles are intercepted by the collimators.

After the acceleration of the beams, the beam losses stay constant during flat top and squeeze (marked in yellow) until the preparation of collisions. Flat top is the mode for checking and preparing the squeeze of the beams. The squeeze process is needed to reduce the transverse size of the beam/bunches at the interaction points by reducing the beta function. If the beta function is reduced the beam size is also smaller (see Sec. 4.2) leading to an increase of the luminosity (see

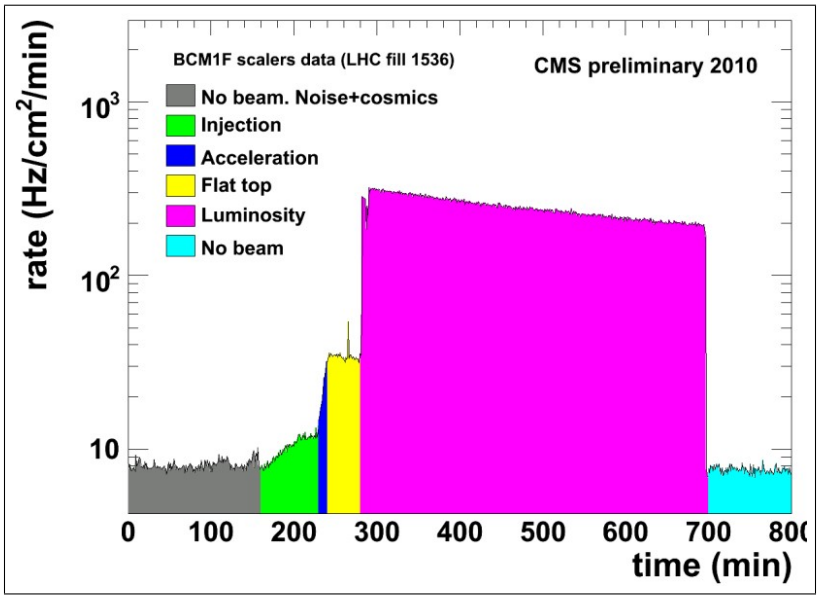

Figure 54: Measurement of Signals per second over time from BCM1F. The different stages of one LHC run is visible (Injection, Ramp, Squeeze, Adjust and Stable Beams) [taken from E. Castro, DESY-Zeuthen].

Sec. 7.4). After the squeeze the beams are adjusted for head-on collisions in CMS with a small crossing angle. Both beams are adjusted and brought into collision right before the stable beam mode (marked in pink). During stable beam condition the beams collide in all the experiments until the beam is dumped by the operator or by a protection beam dump. Beam losses during the stable beam mode are due to the collision products. The bunches in CMS collide head-on with maximum luminosity. Due to a decrease of the beam intensity and an increase of the beam size during the collision process, the scaler rates decrease within the collision process. The scaler rates after the beam dump are again due to noise and cosmic particles (marked in light blue).

8.4.2 Scaler Rates next to LHCb

A scaler measurement for a proton run is shown in Fig. 55. It was done with the sCVD diamond detectors in IR8 and shows beam losses over time during collisions in LHCb. The main difference between beam losses during collisions in CMS and LHCb is that the luminosity in LHCb is constant because the bunches in LHCb collide with an offset to reduce the luminosity (see Sec. 7.4). By changing the offset the luminosity is kept constant over time. Therefore, the scaler rates in IR8 are lower than in CMS and constant during the whole collision process in LHCb.

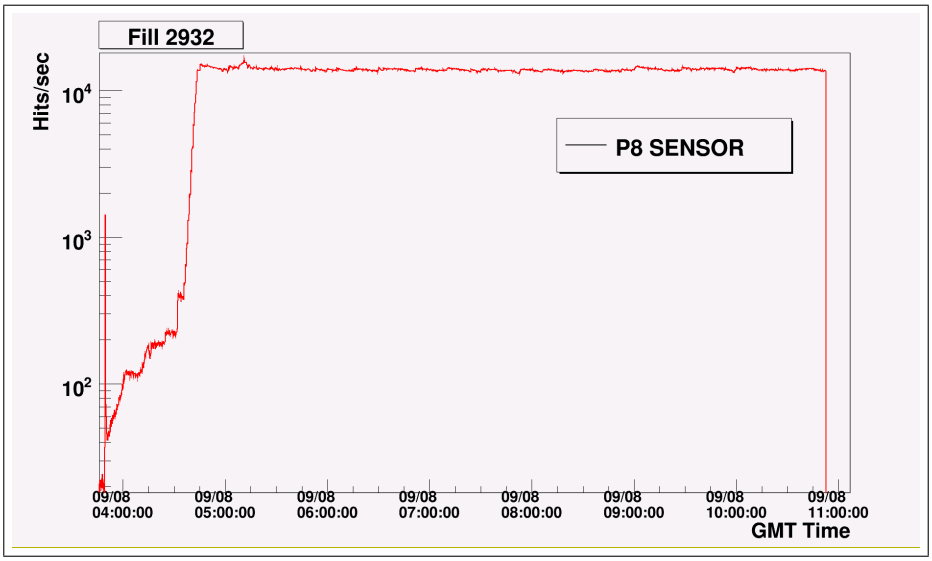

Figure 55: Signals per second from diamond detector in IR8. The luminosity in IR8 is kept constant and therefore the scaler rates are constant during the collision process.

8.4.3 Scaler Rates During van-der-Meer Scan

To calibrate the luminosity, a van-der-Meer scan is needed as explained in Sec. 7.4. During the van-der-Meer scan the bunches collide with an offset that is varied in appropriate steps. The count rates as a function of time during a van-der-Meer scan have approximately a Gaussian shape. This can be understood since steps in time correspond to steps in the offset and the proton density distribution in a bunch is usally described by a Gaussian. The maximum collision rate is obtained when both beams perfectly overlap. Additionally, the vertical and horizontal beam size are determined. These qualities are needed to determine and estimate the cross section as described in Ref. [28].
Figure 56 shows the count rates as a function of time measured with diamond detectors in IR2. The scaler measurement was taken during three van-der-Meer scan in the ALICE experiment. The beam losses during a van-der-Meer scan are Gaussian-like.

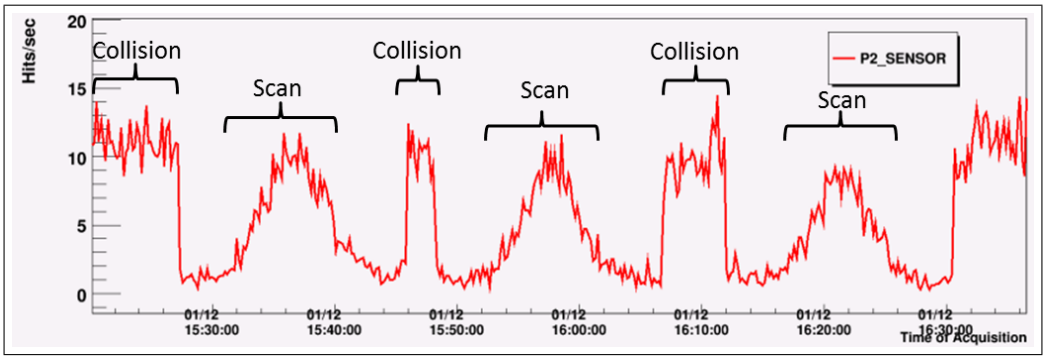

Figure 56: Signals per second over arrival time from IR2. The data was taken during a van-der-Meer scan that leads to beam losses with an approximately Gaussian shape.

9 Comparison of Simulations and Diamond Measurements to other Diagnostic Devices at LHC

9.1 MadX Simulations with Ionization Chamber Measurement

UFO events are one example of beam losses that can appear in the LHC ring and were detected in the cleaning region IR7, as discussed in Sec. 8.1. The predicted locations of beam losses due to an UFO were obtained from simulations and are shown in Fig. 19. The simulation shows that most beam losses appear in the IR7 cleaning region but also in IR2, IR3 and IR6. The simulation was done to reproduce the spatial beam loss pattern around the LHC ring caused by UFO events, appearing at the MKI in region IR2.

Figure 57 shows beam losses measured with ionization chambers around the LHC ring with the same condition[12] as it was used for the simulations. Each spike corresponds to one ionization chamber in the LHC ring. The scale on the y-axis is the information about beam loss rate in Gray per second. Only ionization chambers next to collimators are taken into account since MadX simulates beam losses at collimators. The red lines (marked with dump) illustrate the location of beam losses of ionization chamber that are above the dump threshold. That is the case for ionization chambers in IR2 and IR6. The triggered beam dump in IR2 is due to beam losses from inelastic and elastic scattered particle caused by an UFO that occurs in IR2. The losses in IR6 are mainly due to the unbunched beam that produces beam losses during the beam dump process (see Sec. 8.1.2). The main beam losses measured by the ionization chambers are in IR2, IR3, IR6 and IR7.

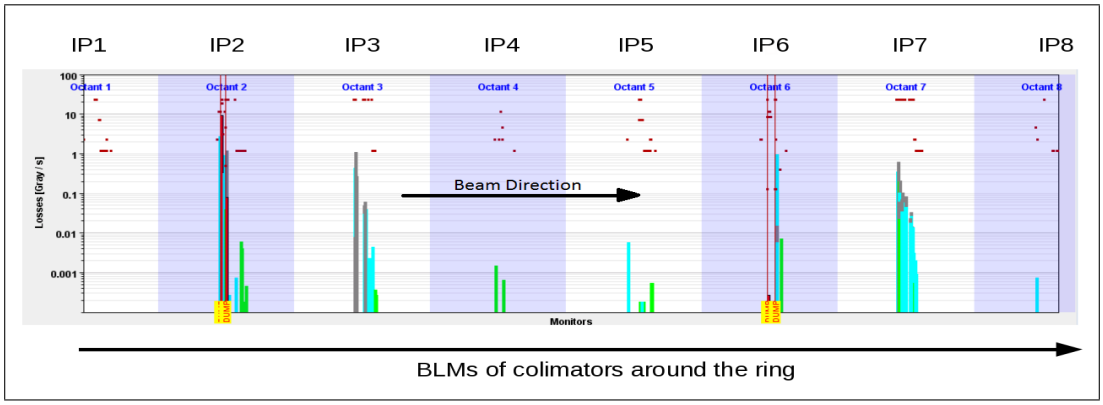

Figure 57: Measured beam losses around the LHC ring. Each spike corresponds to one ionization chamber.

A comparison between the ionization chambers next to collimators with larger beam losses (Fig. 57) to the simulation (Fig. 19) reveal the same beam loss locations even though the MadX simulation is only based on beam losses due to elastic scattering.

MadX tracks all elastic scattered protons around the LHC ring and contains the information about all collimator locations in the LHC. If a proton hits one of the collimator, it is lost and no secondary particles are produced. MadX cannot simulate the interaction of protons with matter and therefore secondary particle showers are not taken into account. Only the loss location of the

[12] The UFO event occured during at a beam energy of 3.5 TeV with injection optics.

proton is provided by the MadX simulation.
In contrary the ionization chambers measure elastic and inelastic scattered particles. Additionally, the ionization chambers detect beam losses due to the lost proton and secondary particles. If a proton hits a primary collimator, it produces a secondary particle shower because of the interaction with matter. Due the multi-stage cleaning (see Sec. 3.4), the secondary particles are intercept by the secondary collimators. That can be observed in the ionization chamber measurement in Fig. 57. The tail structure of the beam loss pattern can be explained by the secondary and tertiary particles that produce signals in the ionization chambers next to secondary and tertiary collimators.
Therefore, the beam losses of secondary particles are visible in the ionization chamber measurement but not in the MadX simulation.
The MadX simulation and the measured beam losses with ionization chambers are qualitatively comparable. Not all signals in ionization chambers can be predicted with MadX due to signals coming from secondary particles but the locations of the main beam losses in the simulation compared to the measured ones show good agreement.
Therefore, the simulation can be used to understand the major beam loss locations around the LHC ring caused by an UFO events in the injection region.

9.2 Scaler Rates with Ionization Chambers

Scaler rates from a sCVD diamond in IR8 during collision are presented in Sec. 8.4. It is explained that the luminosity in LHCb is kept constant during the collision process. Therefore, a constant scaler rate caused by collision products is observed in IR8. Since the diamond detectors are able to see all kind of beam losses it is also possible to observe changes in the vacuum pressure.
In Fig. 58 the luminosity in LHCb for the fill number 2208 is shown. The luminosity is again constant for LHCb.

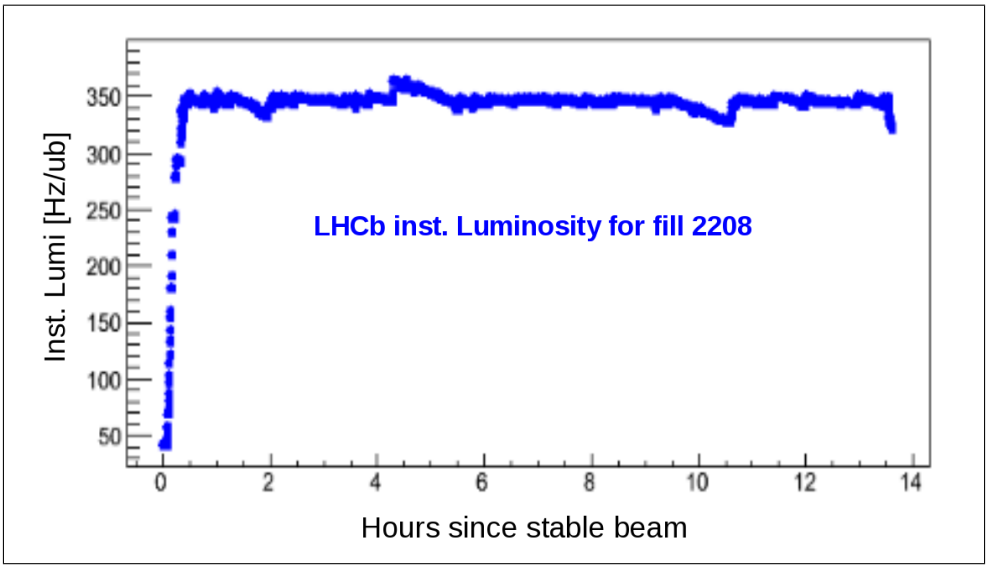

Figure 58: Instantaneous luminosity in LHCb during a collision duration of 14 hours for the fill number 2208. The luminosity in LHCb is kept constant for the whole collision process.

However, the scaler rate of the sCVD diamond in IR8 for the same fill (Fig. 59) shows a different behavior for the beam losses. An increase and decrease during the collision process was detected.

The same observation was done with the ionization chambers for the same fill that is shown in Fig. 60. The beam loss measurement with the ionization chambers that is located next to the diamond detector show the same beam loss shape as a function of time for fill number 2208. Therefore, a faulty beam loss detection with the diamond can be excluded.

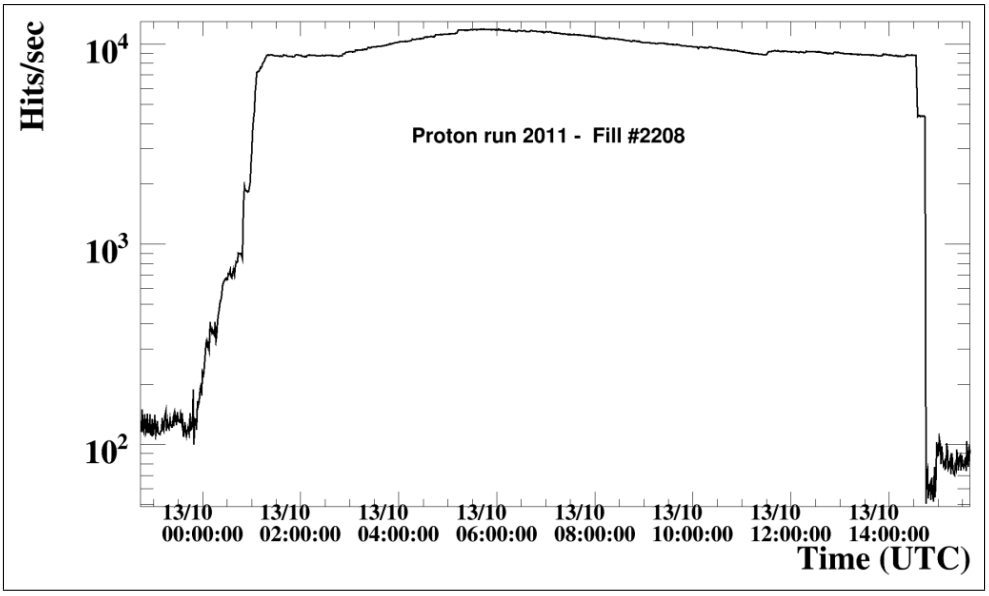

Figure 59: Scaler rates over time from sCVD diamond detector in IR8 for the fill number 2208. An increase and decrease of the scaler rates during collision was observed.

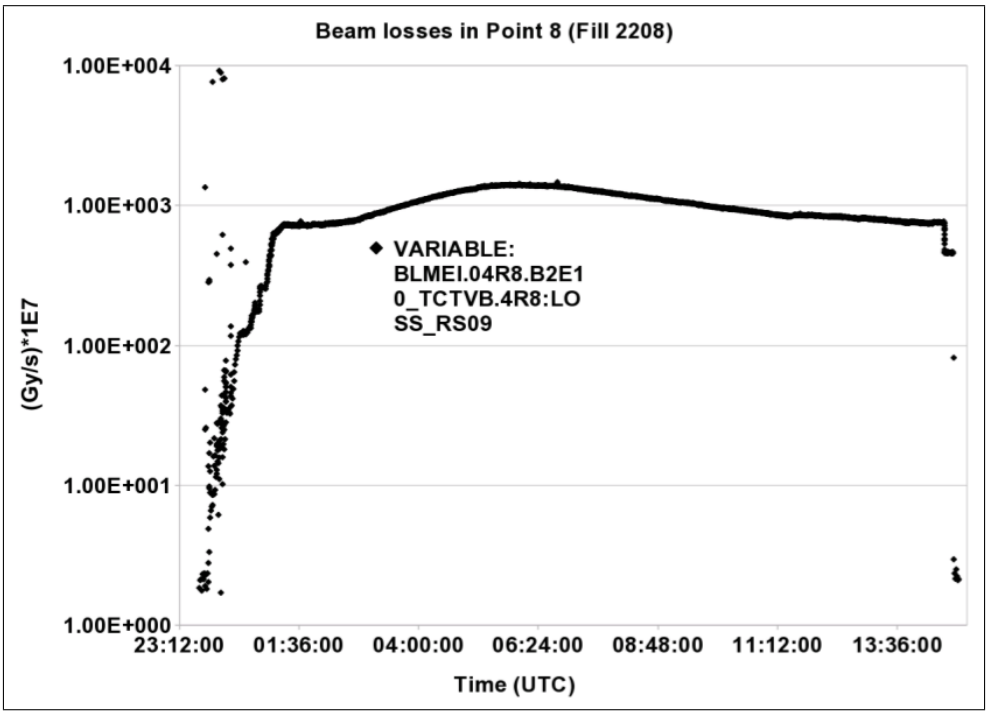

Figure 60: Beam loss measurement of one ionization chambers next to the sCVD diamond in IR8. An increase and decrease of beam losses during collision is visible.

Since the luminosity measurement from LHCb shows a constant collision rate, the scaler counted particles from the collisions and also from beam gas interactions caused by a higher vacuum pressure. When the vacuum pressure in IR8 increases, protons from the beam can interact with residual gas particles which leads to additional beam losses. Therefore, an increase and decrease of the vacuum pressure was observed.
The scaler rates can be used for two different purposes. Firstly, the scaler counts particles from collisions and therefore an estimation of luminosity is possible. Additionally, the scaler can be used to observe the vacuum quality because of beam gas interactions that cause higher beam losses.
The different scaler measurements from the sCVD diamond detectors in the LHC ring are published in the LHC control room and are available via the web on the LHC OP Vistar web page. They may warn LHC operators in case of malfunctioning machine components and helps to find the reason.

9.3 BCM1F with HF Luminosity Measurements

The luminosity in CMS is monitored with several detectors and needed for the calculation of the cross section, it is also important for an optimization of the LHC performance. A fast monitoring is done so far by the Hadron Forward Calorimeter (HF). HF is 11.2 m away from the CMS interaction point and with an outer radius of 130 cm, inner radius of 12.5 cm and a length of 165 cm. It measures the flux of collision products in the very forward region. More information about HF is given in Ref. [38].
An additional luminosity monitor as BCM1F provides an independent measurement allowing a permanent cross check and avoid errors in the measurement due to malfunctioning components. In addition, since the data acquisition of BCM1F is independent of the central CMS data acquisition, BCM1F measures the luminosity before CMS starts data taking or in case the HF is not taking data. Therefore, the development of BCM1F detector as a luminosity monitor is important.
First results are already promising as shown in Fig. 61. It shows the instantaneous luminosity as a function of time measured with HF (in blue) and BCM1F (in green).
The slope at the beginning of the collision process is slightly different for BCM1F and HF luminosity. For the rest of the fill both luminosity measurements agree with better than a percent.
The study of the luminosity measurement with BCM1F is still ongoing. For example, the different slope at the beginning of the collision process must be understood in more detail. However, the results so far are promising and the BCM1F luminosity estimations are published in the CMS control room.

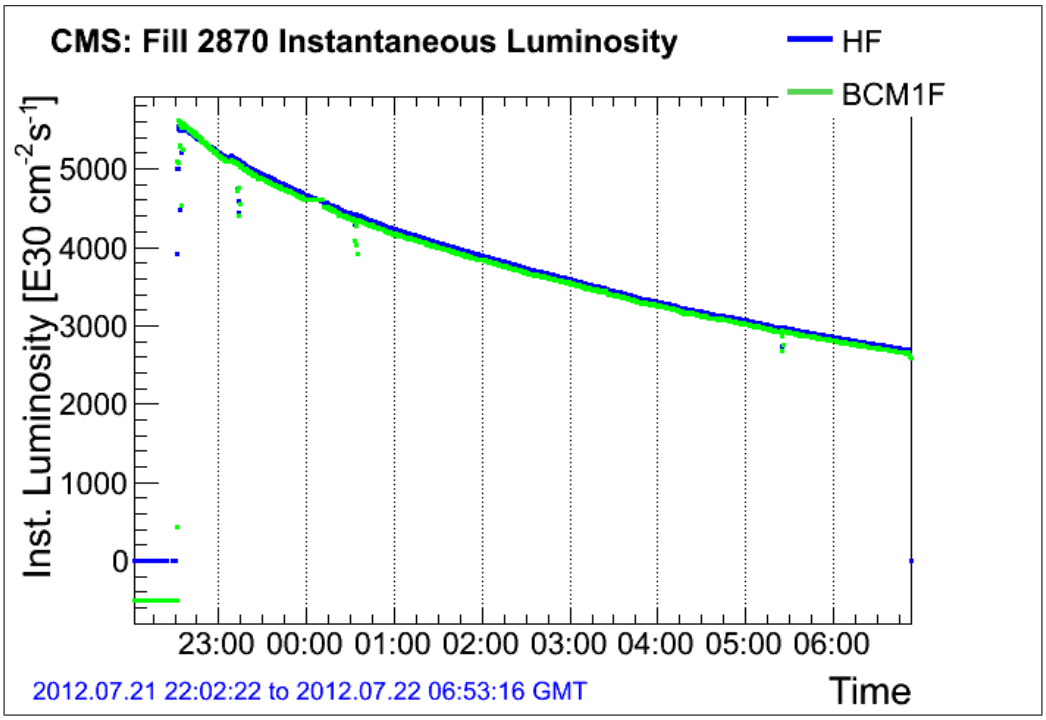

Figure 61: Comparison of luminosity estimation over time between BCM1F scaler rates and HF luminosity.

10 Conclusion

Beam loss monitors in the LHC are indispensable tools to measure beam losses and ensure a safe operation. In the case of larger beam losses above a threshold, the beam is dumped to prevent material damage or magnets from quenching. Different mechanism can lead to beam losses, for example: scattering on residual gas particles (vacuum pressure) or dust particles (UFOs), injection, beam dump, instability or collisions debris from the experiments. To understand the beam loss mechanism in more detail, a beam loss monitor with high time resolution is needed. Therefore, diamond detectors are installed at regions with high beam losses: interaction points of the experiments, injection region, beam dump region and cleaning region. In addition, monitors inside CMS are needed to protect the detector for adverse beam condition. Diamond detectors have a time resolution in the nanosecond range and are radiation hard. With that time resolution it is possible to distinguish beam losses of single bunches or group of bunches at certain locations. A beam loss monitor with a nanosecond time resolution offers a protection system with higher time resolution than the ionization chambers. It also offers a faster reaction time for the protection system in the ns range in case of a beam dump.Detectors using two different diamond detector system are installed in the LHC ring: pCVD diamonds and sCVD diamonds. The two sensors are assembled with different readout modules. The pCVD are read out by an oscilloscope and the sCVD are read out by a data acquisition system including front-end ASICs ADC, TDC and Scaler.
Eight pCVD diamond detectors are installed in the LHC ring. The most important location for diamond detectors is the cleaning region IR7 where the collimators define the global aperture limit. The pCVD diamond detector installed in IR7 detects several kind of beam losses. This thesis presents the observation and analysis of four different cases of beam losses: injection, beam dump, instability and UFO. The most surprising observation was the unbunched beam before the injection of 12 bunches. These losses are due to the circulating probe beam that leads to an unbunched beam and beam losses during the rise time of the injection kicker magnet. Due to the high time resolution of about 1 ns, it is possible to differentiate between the 12 bunches and observe beam losses in each bunch. Beam loss measurements of the beam dump show also losses due to unbunched beam during the rise time of the beam dump kicker magnets. Another measurement shows that only a few bunches become unstable and contribute to beam losses in case of the shown beam instabilities. The beam losses were modulated by the fractional tune of 0.3 . The extraction of the fractional tune offers a tune measurement as a future application for diamond detectors. The observation of the UFO event proved for the first time that UFO events lead to equally beam losses in all bunches. The beam loss pattern over several turns is typically Gaussian as it is shown in previous measurements and publications. A simulation of one UFO event in the injection kicker confirmed the observed spatial loss distribution around the LHC. A comparison between the simulation and measurements of ionization chambers shows good agreement.
It is foreseen to make the measurements with the pCVD more operational and available in the LHC control room because of the large interest in this information. The measurements are important to understand the reason for a beam loss or beam dump. A more detailed analysis of beam losses caused by UFO events is possible which is crucial to understand the dynamics of the process. Additionally, a tune measurement based on the pCVD diamond detector might be possible.
The detectors using sCVD diamonds are installed in CMS and in the LHC ring for monitoring the beam conditions. Eight of them are inside CMS to measure the beam halo and the collision

product rates. Six diamonds around the LHC ring measure the beam losses at different locations. The signals are analyzed using different modules (ADC, TDC and Scaler) and results are presented in this thesis.
The ADC samples the diamond signals and is used for amplitude spectra and arrival time distributions. The amplitude spectra gives information about the noise level and the signal size for single relativistic particles, important to set the threshold of the discriminator and for the long-term monitoring of the performance. The arrival time distribution contains the information about the beam losses due to residual gas particles, beam halo and the collision products over an entire LHC turn. The bunch or collision pattern becomes visible. Amplitude spectra and arrival time information from BCM1F diamonds and sCVD diamonds in the LHC were presented.
The arrival time distribution is also measured with the TDC. The advantage of the TDC is that an online analysis is possible. TDC data was taken from BCM1F diamond detectors in CMS and sCVD diamond detectors in the LHC ring. Different effects were observed with the TDC and especially with data from BCM1F. First, a separation between particles originating from colliding and non-colliding bunches is possible due to the nanosecond time resolution and higher rates of the collision products. Another observation with the TDC is the Albedo effect after each colliding bunch. That is explainable with excitation of the material around the BCM1F sensors including slow neutrons or backscattered particles from the downstream detectors. Slow remaining particles from the decay process cross the BCM1F diamond later. A TDC measurement from IR4 shows the rates of halo and residual gas scattering, without collision products. The bunch pattern of the LHC injection is therefore visible.
Scalers measure particle rates and the evolution of beam losses. Therefore, the scaler data from BCM1F detected the different stages of LHC operation: injection, acceleration, flat top and collision. Each LHC operation mode produces a different amount of beam losses. Scaler rates are sensitive to collision rates but also changes in the vacuum pressure were observed which is shown for the diamond detector in IR8. Additional data from a van-der-Meer scan was taken from IR2, showing a typical Gaussian shape when the beam offset is varied.
The measurement of the BCM1F diamond detectors are already published and used for different applications as luminosity monitoring and background measurements in CMS.
The measurements of the sCVD diamond detectors in the LHC ring are available via the LHC OP Vistar web page and in the CMS and LHC control rooms. The diamond detectors next to CMS monitor particle rates outside of CMS after each collision. Additionally, a back up abort gap monitor is under development with the diamond detectors in IR4 by measuring the beam losses in the abort gap. It is also planned to use a BCM1F diamond detector as a abort gap monitor. The rates during the abort gap are measured by the diamond detectors and compared to the abort gap monitor that is based on the synchrotron light produced by the protons in the abort gap.
In summary, the diamond detectors have different application areas and become more and more important. They deliver valuable information for a safe operation of LHC and the CMS detector. Future applications are already under active investigation (tune measurements, UFO observation, abort gap measurement and luminosity monitors).

List of Figures

List of Tables

References

[1] R. Schmidt et al. Protection of the CERN Large Hadron Collider. *New Journal of Physics*, 8(11):290, 2006.

[2] M. Hempel. Study of the Performance of the Data Acquisition Chain for BCM1F Software Upgrade Study of the Performance of the Data Acquisition Chain for BCM1F Software Upgrade. *Bachelor Thesos, Brandenburg University of Technology, Germany*, 2010.

[3] M. Benedikt et al. *LHC Design Report, Volume III.* CERN, Geneva, 2004.

[4] M. Benedikt et al. Performance of the LHC Pre-Injectors. *HEACC*, 2001.

[5] P. Collier et al. The SPS as Injector for LHC: Conceptual Design. Technical Report CERN-SL-97-007-DI, CERN, Geneva, Mar 1997.

[6] K. Wille. *The Physics of Particle Accelerators: An Introduction.* Oxford University Press, 1996.

[7] S. Baird. Accelerators for pedestrians; rev. version. Technical Report AB-Note-2007-014. CERN-AB-Note-2007-014. PS-OP-Note-95-17-Rev-2. CERN-PS-OP-Note-95-17-Rev-2, CERN, Geneva, Feb 2007.

[8] L. Evans and P. Bryant. LHC Machine. *Journal of Instrumentation*, 3(08):S08001, 2008.

[9] O. Bruenning et al. *LHC Design Report, Volume I.* CERN, Geneva, 2004.

[10] C. Bracco, R. Assmann, and L. Rivkin. *Commissioning Scenarios and Tests for the LHC Collimation System.* PhD thesis, Ecole Polytechnique, Lausanne, Lausanne, 2009. Presented on 29 Jan 2009.

[11] R. Assmann. Operational Experience with LHC Collimation. *Proceedings of PAC09, Vancouver, BC, Canada.*

[12] D.E. Groom and S.R. Klein. Passage of Particles Through Matter. *The European Physical Journal C-Particles and Fields*, 15(1):163–173, 2000.

[13] E. Holzer et al. Beam Loss Monitoring System for the LHC. Technical Report CERN-AB-2006-009, CERN, Geneva, Sep 2005.

[14] T. Baer et al. UFOs in the LHC. In *4th meeting of the CERN Machine Advisory Committee*, 2011.

[15] G. Battistoni et al. The FLUKA Code: Description and Benchmarking. *HSS06*, 03/2007.

[16] A. Ferrari et al. FLUKA: A Multi-Particle Transport Code. *CERN-2005-10*, 10/2005.

[17] T. Baer et al. UFOs in the LHC after LS1. In *Chamonix 2012 Workshop, CERN*, volume 2.

[18] N. Fuster Martinez et al. Simulation Studies of Macroparticles Falling into the LHC Proton Beam. 2011.

[19] T. Baer. update on UFOs: 2012 Observations, Studies and Extrapolations. Presentation from Tobias Baer at the LMC 143 meeting in August 2012, CERN.

[20] M. Seidel. *The Proton Collimation System of HERA*. PhD thesis, Hamburg Univ., Hamburg, 1994.

[21] G. Chiodini. Diamond Particle Detectors for High Energy Physics. In *Advances in Sensors and Interfaces (IWASI), 2011 4th IEEE International Workshop on*, pages 37 –42, june 2011.

[22] R. J. Tapper. Diamond Detectors in Particle Physics. *Reports on Progress in Physics*, 63(8):1273, 2000.

[23] E. Castro. Performance of the Fast Beam Conditions Monitor BCM1F in the CMS Experiment at LHC. *Proceedings of DIPAC2011, Hamburg, Germany.*

[24] Private Communications.

[25] Private Communications.

[26] A.E. Dabrowski et al. The Performance of the Beam Conditions and Radiation Monitoring System of CMS. In *Nuclear Science Symposium and Medical Imaging Conference (NSS/MIC), 2011 IEEE*, pages 489 –495, oct. 2011.

[27] Website. www.allcircuits.com/vol_4/chpt_13/4.html, found on the 23.01.2013.

[28] A. Dabrowski et al. Luminosity Monitoring at CMS During the 2012 Run Using the BCM1F Detector. CMSDN DN-12-006, Draft work still in progress.

[29] S. M. White. Luminosity Scans at the LHC. *LHC Lumi Days 2011, CERN, Geneva, Switzerland.*

[30] S. van der Meer. Calibration of the Effective Beam Height in the ISR. Technical Report CERN-ISR-PO-68-31. ISR-PO-68-31, CERN, Geneva, 1968.

[31] A. Dabrowski. Beam Backgrounds and Online Luminosity at 8 TeV. Presentation from Anne Dabrwoski during the Physics Week April 2012.

[32] M. Hempel et al. Bunch-by-Bunch Beam Loss Diagnostics with Diamond Detectors at the LHC. *HB 2012, Beijing, China, MOP203*, 2012.

[33] V. Kain et al. Injection Beam Losses and Beam Quality Checks for the LHC. *Proceedings of IPAC 2010, Kyoto, Japan, TUPEB066*, 2010.

[34] M. Meddahi et al. LHC Abort Gap Monitoring and Cleaning. *Proceedings of IPAC 2010, Kyoto, Japan, MOPEC009*, 2010.

[35] E. Metral. Overview of Impedance and Single-Beam Instability Mechanism. *Proceedings of PAC 2005, Knoxville, USA, CERN-AB-2005-041*, 2005.

[36] R. Walsh. Performance of the CMS Fast Beam Conditions Monitor. In *Nuclear Science Symposium Conference Record (NSS/MIC), 2010 IEEE*, pages 1569 –1572, 30 2010-nov. 6 2010.

[37] S. Muller, W. Boer, and T. Muller. *The Beam Condition Monitor 2 and the Radiation Environment of the CMS Detector at the LHC*. PhD thesis, Karlsruhe, U., Karlsruhe, 2011.

[38] A. Penzo, Y. Onel, and the CMS Collaboration. The CMS-HF Quartz Fiber Calorimeters. *Journal of Physics: Conference Series*, 160(1):012014, 2009.

Acknowledgment

Foremost, I have to thank you my supervisor and professor Wolfgang Lohmann. He supported my work since several years. He gave me the chance to work for his CMS research group in DESY-Zeuthen and he gave me the opportunity to write my Bachelor thesis about the project BCM1F. The work for BCM1F provided me an insight into detector physics and also the knowledge about analysis and hardware of a detector. Due to the support of Wolfgang Lohmann and Wolfram Zeuner, I got the chance to work at CERN as a Technical Student. I am really grateful for that opportunity because the time at CERN was an experience that I do not want to miss. I met nice people, colleagues and friends who are helping and supporting me at any time.
During the time at CERN, I had the pleasure to work together with fantastic people and an exceptional group leader who has always new and interesting ideas, Rüdiger Schmidt. The work in his group gave me an insight in a new field of physics, accelerator physics. He also gave me the opportunity to write my first publication about the measurements and analysis that I did in his group. I really thank you for that support.
The publication and measurements would not be possible without the help of Tobias Bär. He took his time to answer every question, especially in accelerator physics and LHC operation. I learned quite a lot about the operation of the LHC due to discussions with him and measurements that we did. I was also very impressed by his commitment to work at any time.
A special thank you goes to the DESY-Zeuthen group and BRM group at CERN. It was and still is a pleasure for me to work together with people from both groups because of their readiness to help. I enjoyed the working in both groups because it covers a large range of knowledge about hardware and software.

I also want to thank my family, especially my parents who supported me during the university time. They made it possible that I could study without interruptions. Additionally, they always listen to my problems and give me always a helpful advices. Last but not least I want to say “ thank you ” to Hannes. He supports all my decisions that I take and listens to my worries. Hannes became a very important person in my life because of his love and support. I have never met a person with so much understanding.

At the end I want to thank every body who supported me. I learned in the past five years that support is the most important thing in life. Success in work and happiness in life would not be possible without support of supervisors, colleagues, family and friends.